



저작자표시-비영리-변경금지 2.0 대한민국

이용자는 아래의 조건을 따르는 경우에 한하여 자유롭게

- 이 저작물을 복제, 배포, 전송, 전시, 공연 및 방송할 수 있습니다.

다음과 같은 조건을 따라야 합니다:



저작자표시. 귀하는 원저작자를 표시하여야 합니다.



비영리. 귀하는 이 저작물을 영리 목적으로 이용할 수 없습니다.



변경금지. 귀하는 이 저작물을 개작, 변형 또는 가공할 수 없습니다.

- 귀하는, 이 저작물의 재이용이나 배포의 경우, 이 저작물에 적용된 이용허락조건을 명확하게 나타내어야 합니다.
- 저작권자로부터 별도의 허가를 받으면 이러한 조건들은 적용되지 않습니다.

저작권법에 따른 이용자의 권리는 위의 내용에 의하여 영향을 받지 않습니다.

이것은 [이용허락규약\(Legal Code\)](#)을 이해하기 쉽게 요약한 것입니다.

[Disclaimer](#)

공학석사 학위논문

**Study on the Entropic Contribution to
Electrochemical Water Oxidation
Catalysis**

전기화학적 물 산화 반응 중 엔트로피
기여에 관한 연구

2019 년 2 월

서울대학교 대학원

재료공학부

이 강 규

Abstract

Study on the Entropic Contribution for Electrochemical Water Oxidation Catalysis

Kang-Gyu Lee

Department of Materials Science and Engineering

The Graduate School

Seoul National University

Artificial photosynthesis is one of the crucial strategies for sustainable energy production. The oxygen evolution reaction (OER), which is an important part of artificial photosynthesis, shows sluggish reaction kinetics due to the high energy barrier, and accordingly, the development of highly active catalysts is essential. To date, the origins of enthalpy of activation ($\Delta^\ddagger H$) of high energy barrier ($\Delta^\ddagger G$) has been well understood, and various strategies have been proposed to reduce the activation enthalpy. In this approach, scientists are focusing on the control of binding

energy with intermediate species (*O, *OH, and *OOH). However, not only catalytic properties of artificial electrocatalysts are still far below than oxygen evolving enzyme (photosystem II), but also there is a theoretical limitation in improvement of activities by scaling relation.

In nature, all of the various biochemical reactions are regulated by enzymes, which lower the activation energy barrier of reactions, and crucially enhance the reaction kinetics even in mild condition. The origins of fast kinetics of enzyme have been identified as favorable entropy of activation ($\Delta^\ddagger S$). For the water oxidation, favorable entropy effect of Ca^{2+} and amino-acid residue in Mn_4Ca cluster has been reported as a decisive parameter for oxygen evolving kinetics. Furthermore, entropic contribution in molecular catalyst has been investigated based on the understanding about enzyme catalysis. However, in the heterogeneous water splitting, effect or origins of $\Delta^\ddagger S$ is not clearly identified, and overlooked because of difficulties in measuring and calculating $\Delta^\ddagger S$.

Here, we propose the methodology for measuring activation energy parameters including activation enthalpy ($\Delta^\ddagger H$) and entropy ($\Delta^\ddagger S$) for oxygen evolution reaction (OER) on Mn_3O_4 NPs and Co-Pi film through the temperature dependent kinetic analysis. In our results, measured $\Delta^\ddagger H$ linearly decreased with overpotential in proportion to the transfer coefficient (α). The transfer coefficient of Mn_3O_4 NPs, and Co-Pi were measured to 0.74, and 0.96 respectively, which is consistent with previously reported results. Also, $T\Delta^\ddagger S$ was successfully measured to -0.46 – -0.49 eV for Mn_3O_4 NPs, and -0.4 eV for Co-Pi, which accounts for a larger portion of the whole activation Gibbs free energy ($\Delta^\ddagger G$) than $\Delta^\ddagger H$. Considering entropy values of intermediate species calculated by DFT studies, we confirmed that

this negative entropic contribution could be possible by nucleophilic attack of H₂O molecule in the process of O-O bond formation. Further, we propose that activation entropy can be reduced by hydrogen-bond between Co-OOH and adjacent Co-OH in case of Co-Pi. In this study, we proposed that entropy contribute highly unfavorable to reaction kinetics and suggested entropy as crucial key kinetic factor in heterogeneous OER. In addition, we proposed that highly negative entropic contribution could be originated from mechanistic aspect, mainly nucleophilic attack of water molecule during O-O bond formation.

Keywords: Oxygen evolution reaction, Transition state theory, Temperature dependent analysis, Electrochemical study, Entropy, O-O bond formation, Manganese oxide, Cobalt phosphate

Student Number: 2017-24770

Contents

Abstract.....	i
Contents.....	iv
List of Tables.....	viii
List of Figures.....	ix
Chapter 1. Introduction.....	1
1.1 Demand for Hydrogen Energy	1
1.2 Electrochemical Oxygen Evolution Reaction (OER).....	3
1.2.1 The necessity for the development of OER catalyst.....	3
1.2.2 Catalytic mechanism of OER.....	4
1.2.3 ‘Design Rule’ for artificial catalyst.....	7
1.3 Water Oxidation Enzyme in Nature: Photosystem II.....	10
1.3.1 Photosystem II (PS II) in biological system.....	10
1.3.2 Oxygen evolving complex (OEC) in PS II.....	11
1.3.3 Hydrogen-bond network and protein channel in OEC.....	14
1.3.4 Entropic contribution to water oxidation in PS II	18
1.4 Enzyme Catalysis in Nature.....	23

1.4.1	Favorable entropic contribution of enzyme catalysis.....	24
1.5	Artificial Electrocatalysts for Water Oxidation.....	28
1.5.1	Bioinspired Mn based Catalyst.....	28
1.5.2	Computational entropic consideration in DFT study.....	29
1.5.3	Experimental measurement of entropy.....	33
1.5.4	Transition state theory for electrochemical OER.....	35
1.6	Objective of the Thesis.....	41
 Chapter 2. Experimental and Procedure.....		45
2.1	Preparation of Catalysts.....	45
2.1.1	Materials.....	45
2.1.2	Manganese oxide nanoparticles (Mn ₃ O ₄ NPs).....	46
2.1.3	Cobalt phosphate (Co-Pi).....	49
2.2	Characterization	50
2.2.1	Powder X-ray diffraction (XRD).....	50
2.2.2	Scanning electron microscopy (SEM).....	50
2.2.3	Transmission electron microscopy (TEM).....	51
2.3	Electrochemical Methods	52
2.3.1	Cyclic voltammetry (CV) measurements.....	52
2.3.2	Tafel slope analysis.....	52

2.3.3	Temperature dependent electrochemical measurements.....	53
2.3.4	Electrochemical active surface area (ECSA).....	54
Chapter 3. Results and Discussion		57
3.1	Set-up the Electrochemical Cell.....	57
3.2	Characterization of Catalysts.....	60
3.2.1	Manganese oxide nanoparticles (Mn ₃ O ₄ NPs).....	60
3.2.2	Cobalt phosphate (Co-Pi).....	63
3.3	Electrochemical Characterization.....	65
3.4	Investigation of Entropic Contribution.....	68
3.4.1	Temperature dependent kinetic analysis.....	68
3.4.1.1	Analysis on the enthalpy of activation ($\Delta^\ddagger H$).....	71
3.4.1.2	Analysis on the entropy of activation ($\Delta^\ddagger S$).....	75
3.4.2	Entropic contribution to O-O bond formation during water oxidation	85
Chapter 4. Conclusion		89

References.....91

국문 초록.....103

감사의 글.....106

List of Tables

Table 1.1	Measured activation energetic parameters for various enzyme reaction. Gibbs energy of activation ($\Delta^\ddagger G$) decreased by enzyme, and measured $\Delta^\ddagger H$ and $\Delta^\ddagger S$ showed it was derived from entropic contribution, not enthalpic contribution.....	27
Table 1.2	Reported TS (eV) from the DFT study for various materials (T=25°C).....	31
Table 1.3	Measured activation parameters ($\Delta^\ddagger H$ and $\Delta^\ddagger S$) through temperature dependent kinetic analysis in heterogeneous and homogeneous catalyst systems (*T = 25°C).....	34
Table 1.4	Comparison of kinetic equation and energetic parameters which can be measured from temperature dependent analysis between Arrhenius and Eyring model.	44
Table 3.1	Temperature dependent Tafel slope of Mn ₃ O ₄ NPs, and Co-Pi.....	70
Table 3.2	Reported the number of active site for nano-sized metal oxide catalysts for OER	79

List of Figures

- Figure 1.1** Schematic representation of water oxidation mechanism (a) Acid-Base (AB) mechanism for O-O bond formation (b) Radical-Coupling (RC) mechanism for O-O bond formation.....6
- Figure 1.2** Volcano plots between catalytic activities and proposed descriptors. (a) Activity trends towards oxygen evolution. The negative values of theoretical overpotential were plotted against the standard free energy of $\Delta G_{\text{HO}^*} - \Delta G_{\text{O}^*}$ step. (b) The relation between the OER catalytic activity and the occupancy of the e_g -symmetry electron of the transition metal (B in ABO_3).....9
- Figure 1.3** Overall structure of PS II at a resolution of 1.9 Å and structure of OEC involving the Mn_4Ca cluster and surrounding proteins.....13
- Figure 1.4** Hydrogen-bond networks surrounding OEC. (a) H-bond around Yz. Solid line depicts the bond between metal and water molecules, and H-bonds are represented as dashed lines. (b) H-bond networks from Mn_4Ca cluster to luminal bulk phase.....16
- Figure 1.5** Proposed water channels and surrounding amino-acid residues. Circled Asp61, Val185 and Ca^{2+} in Mn_4Ca cluster play central roles to make entropic contribution favorable.17
- Figure 1.6** The entropic contribution in formation of intermediate species during

$S_2 - S_3$, and $S_3 - S_0$ transition. (a) The kok cycle of photosynthetic oxygen evolution. (b) Energetic schemes for $S_2 - S_3$, and $S_3 - S_0$ transition.....21

Figure 1.7 Increase of energy barrier for mutant PSII due to the unfavorable entropic contribution. Substitution of Ca^{2+} to Sr^{2+} induces the decrease activation entropy ($T\Delta^\ddagger S$) by disturbing the formation of ordered transition state prior to O-O bond formation. Two amino-acid residues (Asp61 and Val185) consist of water channel, and substitution of Asp to Asn (D61A) and Val to Asn (V185N) also induce the decrease of $T\Delta^\ddagger S$22

Figure 1.8 Scheme which represents the entropic contribution in enzyme reaction. Favorable entropic contribution in enzyme reaction has been explained by two theories. First, required entropic energy barrier decrease due to the loss of vibrational entropy of substrate during the enzyme-substrate binding. In addition, transition state could be stabilized in enzyme by H-bond networks or pre-organized surrounding proteins.....26

Figure 1.9 TAS diagram based on the DFT calculation. Co-OH is initial state and Co=O is formed by deprotonation step. After that, O-O bond formation step is following through acid-base mechanism (AB mechanism) and radical coupling mechanism (RC mechanism). RC mechanism has positive entropic contribution due to the

deprotonation step. On the other hand, highly negative activation entropy ($T\Delta^\ddagger S$) is required in nucleophilic attack of H₂O in O-O bond formation (T=25°C).....32

Figure 1.10 Free energy diagram of typical electrochemical oxygen evolution reaction. It is assumed that reaction is proceeded by acid-base mechanism, and O-O bond formation step is rate determining step (RDS). The experimentally measured activation parameters are the difference of energy state between initial state and transition state of RDS. Red bar and black bars represent the free energy of activated species in RDS, and free energy of intermediate species at standard electrode potential (E°), respectively. Blue bars represent the free energy of intermediates when overpotential (η) is applied.....40

Figure 1.11 Butler-Volmer equation and Eyring plot for electrochemical reaction. ($\Delta^\ddagger G$: Gibbs free energy of activation, $\Delta^\ddagger H$: enthalpy of activation, $\Delta^\ddagger S$: entropy of activation, α : transfer coefficient and Γ_{act} : the number of active site).....43

Figure 2.1 Scheme for synthesizing manganese oxide nanoparticles by hot injection method.....47

Figure 2.2 Scheme for preparing manganese oxide nanoparticles film.....48

Figure 2.3 Scheme for methodology to control W.E. versus RHE in neutral condition. In gas/electrolyte interface, we can directly measure W.E. vs. RHE without liquid junction potential.....56

Figure 3.1	(a) Liquid junction potential in acidic solution based R.H.E system. (b) Validation of hydrogen electrode system in neutral condition. Ag/AgCl (KCl 3M) electrode was used as working electrode and gas diffusion RHE was used as reference electrode. Every points were measured by open circuit potential measurement.....	59
Figure 3.2	The XRD pattern of powder Mn ₃ O ₄ NPs. Black bar represents the reference PDF card of Mn ₃ O ₄ (PDF #: 00-024-0734).....	61
Figure 3.3	Electron microscopic images of Mn ₃ O ₄ NP. (a-b) TEM image of synthesized Mn ₃ O ₄ NPs. Inset of (b) shows a high resolution image of the Mn ₃ O ₄ crystal. (c-d) Plane and cross sectional SEM images of Mn ₃ O ₄ NPs films on FTO substrates.....	62
Figure 3.4	Characterization of Co-Pi films by SEM (a) Plane SEM image for Co-Pi film. (b) SEM-EDS histogram for deposited Co-Pi film.	64
Figure 3.5	Electrokinetic characterization of Mn ₃ O ₄ NPs and Co-Pi. (a) Polarization curve and (b) Tafel slope in neutral condition (pH 7).....	67
Figure 3.6	Temperature dependent kinetics of OER. Polarization curves (a) and Tafel slope (b) of Mn ₃ O ₄ NPs, and (c, d) Co-Pi.....	69
Figure 3.7	Eyring plot for (a) Mn ₃ O ₄ NPs, and (b) Co-Pi from 20°C to 70°C.....	73
Figure 3.8	Confirmation of measured transfer coefficient (α). Potential dependent enthalpy of activation ($\Delta^\ddagger H$) for (a) Mn ₃ O ₄ NPs, and (b)	

Co-Pi. α was measured by Butler-Volmer equation. (c) Measured α in our work and Tafel slope analysis. Accordance of α reflect the reliability of these kinetic analysis.....74

Figure 3.9 (a) Our proposed circuit model for impedance analysis for Mn_3O_4 NPs film. R_{tr} indicate resistance for electron transport in the film. The R_{int} and C_{int} in RC loops, which are described surface catalysis, mean interface resistance and capacitance, respectively. (b) Comparison of rate constant (k) from our model and reported values.....77

Figure 3.10 Double layer capacitance measurement for determining ECSA analysis for (a, b) Mn_3O_4 NPs. (a) Cyclic voltammetry were measured in a non-Faradaic region at various scan rate. (b) The cathodic and anodic charging currents measured at 0.45 V vs. Ag/AgCl. The determined double-layer capacitance of the system is represented.....81

Figure 3.11 Measured y-intercepts in Eyring plot for Mn_3O_4 NPs, and Co-Pi. In low overpotential, y-intercepts were obtained within similar ranges and average value was used in analysis.....83

Figure 3.12 Calculated $T\Delta^\ddagger S$ from the temperature dependent analysis for (a) Mn_3O_4 NPs and (b) Co-Pi. Blue line is calculated number of active site (Γ_{act}), and Red line is calculated $T\Delta^\ddagger S$ ($T = 25^\circ C$).....84

Figure 3.13 Comparison of entropy change in O-O bond formation mechanism for cobalt based catalyst. (a) Two possible mechanisms of O-O bond

formation on Mn_3O_4 NPs. (b) Calculated TS diagram for acid-base, and radical-coupling mechanism. S_0 is calculated entropy value at initial state ($T = 25^\circ\text{C}$).....86

Figure 3.14 Proposed mechanisms of O-O bond formation during OER on cobalt based catalysts. Two types of acid-base mechanisms were reported by Frei group. The one is slow cycle by single Co site and the other is fast cycle by dual Co site. Radical-coupling mechanism was reported by Nocera group.....88

Chapter 1. Introduction

1.1 Hydrogen Energy Future

1.1.1 Demand for hydrogen energy

Development of sustainable energy system is one of the crucial challenges facing human society. International Energy Agency reported that among the global energy demand in 2013 (18 TW), 80 % of which were provided from fossil fuel resources (coal, oil, and gas)¹. This severe dependency on fossil fuels has been suggested to a major cause of global warming. As world population increases and industrialization expands, world energy demand is projected to double from 13.5 TW in 2001 to 27 TW by 2050 and to triple to 43 TW by 2100.² As a result, there has been a major interest in energy supply with regard to environmentally friendly pathway.

Hydrogen energy is one of the most promising renewable energy resource among various candidate. Hydrogen has high energy density (142 kJ/g) compared to gasoline (46 kJ/g) and natural gas (47.2 kJ/g).³ Also, it is non-toxic and produces water as by-product. Furthermore, as the cost of fuel cell system which use hydrogen as energy resource has been reducing, demand for hydrogen energy is predicted to increase.

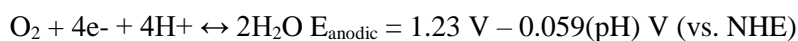
At present, the vast majority (96 %) of hydrogen is produced by gas reforming method. In this method, syngas, which is converted from natural gas (48 %), oil (30 %), and coal (18 %) via thermochemical conversion, is decomposed to hydrogen and carbon monoxide in high temperature³. This method has crucial disadvantage that it produces CO and CO₂ as byproduct and high energy should be consumed in high temperature condition. As the demand for hydrogen energy increases, research on the development of environmental-friendly hydrogen energy production methods is essential.

1.2 Electrochemical Oxygen Evolution Reaction (OER)

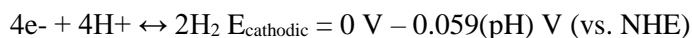
1.2.1 Water splitting and necessity of OER catalyst

Electrochemical water splitting is environmentally friendly hydrogen production method. Unlike gas reforming method, water splitting has advantages that hydrogen can be produced in ambient condition and only oxygen molecules are generated as by-product. Basically, water splitting consists of two half reaction as described below.

i) Water oxidation reaction (Oxidation reaction)



ii) Hydrogen evolution reaction (Reduction reaction)



Hydrogen evolution reaction occur in cathode, and oxygen evolution reaction occur in anode site. Although there is an advantage of producing hydrogen without additional gas reforming process, electrochemical hydrogen production has challenge which is high overpotential of oxygen evolution reaction. Among both reaction, oxygen evolution reaction (OER) is kinetically sluggish and limit overall efficiency of water splitting. It is because OER contains four electron transfer step and involve the high activation energy barrier for O-O bond formation. Therefore,

development of outstanding OER electrocatalysts is essential to enhance efficiency of whole water splitting reaction, which means efficient hydrogen production.

1.2.2 Catalytic mechanism of OER

As described above, OER is sluggish reaction in which four electrons are transferred, and has three reaction intermediates species in the course of oxidation of water to oxygen. OER is composed of H₂O adsorption step, deprotonation steps to make active O species such as double oxo (M=O) or oxo radical (M-O*), O-O bond formation step, and O₂ liberation step. Due to the high energy level of O-O bond, O-O bond formation is rate determining step for novel metal oxide and some of transition metal oxide such as cobalt phosphate⁴ and manganese oxide nanoparticles⁵. For the most of transition metal oxide in which high valent state is unstable, electrochemical oxidation to form M=O or M-O* is rate determined step⁶. These catalysts show high overpotential and high Tafel slope.

Most interesting issue in water splitting is how O-O bond formation occur during the reaction. Typically, two types of mechanisms are reported for the O-O bond, that is Acid-Base mechanism (AB mechanism) and Radical coupling mechanism (RC mechanism). In AB mechanism, water molecule in the bulk electrolyte attack the high valent oxo species to form M-OOH species. However, in RC mechanism, two oxo radical (M-O*) on the catalysts are involved in O-O bond

to form M-OO-M species. AB mechanism were regarded as energetically favor path way based on the DFT studies for various materials. For example, Liu and Fang reported that AB mechanism had lower energy barrier in high overpotential in RuO₂.⁷

In addition to DFT calculation, experimental investigations of O-O bonding formation have been reported. For the cobalt oxide, Co(IV)-OOH intermediate was captured through time-resolved FTIR by Frei's group.⁸ In his paper, he observed that there are two active pathways that one is fast cycle by dual Co edge site, and another is slow cycle by single Co site. The cooperative effect of adjacent electronically coupled Co(IV)=O sites was proposed, which is absent in the H₂O addition reaction at the slow site. However, For the cobalt phosphate catalyst known as amorphous cobalt oxide nanoparticle, radical coupling between the cobalt(III) oxo radical was proposed by Nocera's group through ¹⁸O isotope experiment.⁹ Moreover, recent DFT studies by Wang and his co-workers, oxo hopping mechanism was proposed.¹⁰ In this mechanism, Co(IV)=O species on the surface of catalyst are hopping by redox reaction with neighboring Co(III)-OH. Through the calculation, they reported O-O bonding formation by nucleophilic attack of water molecules are favor energetically then radical coupling mechanism.

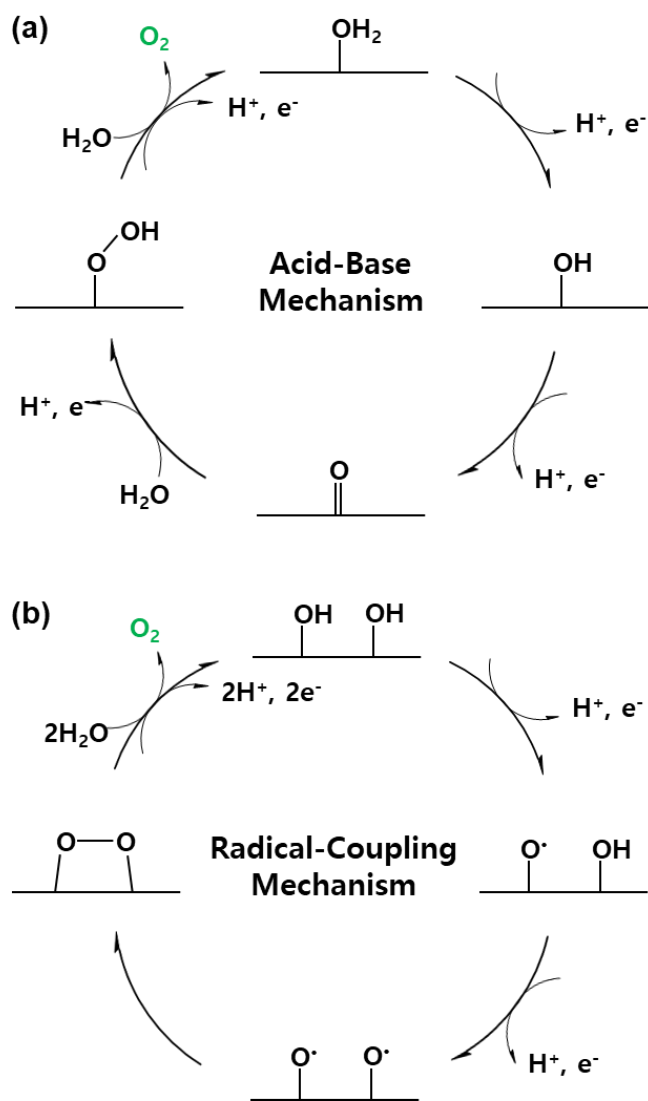


Figure 1.1 Schematic representation of water oxidation mechanism (a) Acid-Base (AB) mechanism for O-O bond formation (b) Radical-Coupling (RC) mechanism for O-O bond formation.

1.2.3 ‘Design rule’ for artificial OER catalyst

Heterogeneous electrochemical reaction involves various complex phenomena, which makes rational design difficult. Therefore, many research has been conducted to identify and develop valid ‘descriptor’ which means key parameter that is principally responsible for the catalytic activity. Reported thermodynamic and kinetic ‘descriptors’ were summarized in this chapter.

In the DFT calculation study, Norkov, Rossmeisl and co-works suggested the origins of the overpotential of OER.¹¹ First, binding energy between catalytic active site and reaction intermediates (*O, *OH and *OOH) is parameters for gibbs energy of intermediate species. Thermodynamic energy barrier is calculated by difference between reaction intermediates and the reaction step having highest energy barrier becomes the RDS. Interestingly, the binding energy with O, OH, and OOH for various metal and metal oxide catalyst has linear dependency where E_{OOH} vs. E_O and E_{OH} vs. E_O have slopes close to 0.5.¹² It means that the catalyst having high binding affinity with *OOH, also bind strongly with *O or *OH. As shown in Figure 1.2a, the volcano plot for catalytic activities were presented and proposed that materials having proper binding energy with intermediates are highly active for OER.¹³

In addition to binding energy, Yang Shao-Horn and co-worker suggested the e_g occupancy as descriptor for OER.¹⁴ Their approach was based on the molecular orbital bonding framework. They reported that the binding with oxygen related intermediate species was highly affected by the occupancy of e_g orbital. The reason was that the e_g orbital of surface transition metal ions participates in σ -bonding with a surface-anion adsorbate. In Figure 1.2b, volcano shaped plot can be also shown according to the electronic density of e_g electron, and the materials having proper e_g electron occupancy showed superior activities for OER.

Recently, however, Over and many scientists insisted that thermodynamically defined overpotential has limitation for anticipating catalytic activities.¹⁵ In his study, Over showed the potential determined step is not always equal with rate determined step, and presented DFT calculation results more matched with experimental results. However, considering kinetic parameters such as transition state or solvent effect is still challenging.

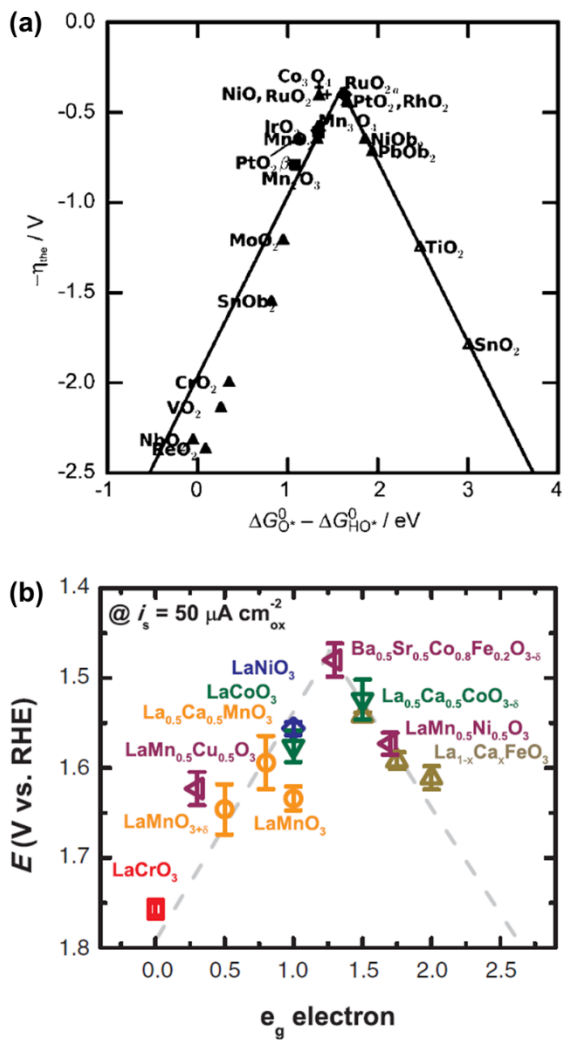


Figure 1.2 Volcano plots between catalytic activities and proposed descriptors. (a) Activity trends towards oxygen evolution. The negative values of theoretical overpotential were plotted against the standard free energy of $\Delta G_{\text{HO}^*} - \Delta G_{\text{O}^*}$ step.¹³ (b) The relation between the OER catalytic activity and the occupancy of the e_g -symmetry electron of the transition metal (B in ABO_3).¹⁴

1.3 Water Oxidation Enzyme in Nature: Photosystem II

1.3.1 Photosystem II (PS II) in biological system

Photosystem II (PS II) is water oxidation enzyme located in the thylakoid membranes of photosynthetic organisms. The overall structure of PS II is shown in Figure 1.2.¹⁶ Through a series of light induced electron transfer reactions, PS II oxidize water molecules to protons and molecular oxygen with redox-active tyrosine residue (Tyr161, Y_z), oxidized by light absorption from P680 reaction center.



Like other enzymes in nature, PS II exhibits superior catalytic properties to artificial catalysts for oxygen evolution reaction. According to previous study, turnover frequency (TOF) value of PS II is around 50 O₂ molecules per second at 60 mV overpotential.¹⁷ In order to develop artificial catalyst having properties close to PS II, fundamental challenge is to understand the mechanistic features of lowering energy barriers. In this section, we will discuss the entropic effect on the unprecedented efficiency of water oxidation catalysis.

1.3.2 Oxygen evolving complex (OEC) in PS II

Active site of water oxidation in PS II is oxygen evolving complex composed of a Mn_4CaO_5 inorganic cluster ligated by waters and amino-acid side chains. In 2011, the structure of Mn_4Ca cluster in S_1 state successfully resolved at a resolution of 1.9 Å through X-ray diffraction technique.¹⁶ As shown in Figure 1.3, Mn_4CaO_5 cluster reveal distorted cubane Mn_3CaO_4 with dangling forth Mn and fifth O (O5). In the Mn_3CaO_4 cubane, O5 has longer bond length with Mn4, Mn3, Mn1 and Ca ion. In addition, four water molecules are coordinated in Mn_4CaO_5 cluster. Two water molecules (W1, W2) are associated with dangling Mn_4 with bond length of 2.1-2.2 Å and other two water molecules (W3, W4) coordinated to Ca in the cubane structure. Two of these water molecules may participate in the water oxidation as water substrates.

Mn_4Ca cluster is surrounded by various amino-acid residues. In the first coordination sphere, amino-acid residues such as D1-G189 and D1-Asp170 directly ligated with Mn_4Ca cluster. These structure may have important effect in the water oxidation mechanisms and O-O bond formation. In the distance further from Mn_4Ca cluster than first coordination sphere, several amino-acids are located in the second coordination sphere and they play an important role in maintaining structure and forming hydrogen-bond networks in OEC which are crucial part in OER activities.²⁰ Tyrosine residue (D1-Tyr161 or Yz) located between the Mn_4Ca cluster and PS II

reaction centre mediates electron transfer between two species.

There are two Cl ion in the vicinity of the Mn₄Ca cluster. These two Cl⁻ surrounded by two water molecules, amino-acid and backbone nitrogen are presumed that they function to maintain the coordination environment of Mn₄Ca cluster.²⁰ As well as structural roles, considering Cl ion are involved in hydrogen-bond with a surrounding water and proteins, they may participate in transferring proton out or water into the Mn₄Ca cluster. The roles of hydrogen-bond network and channels in OEC will be discussed in detail in the next section.

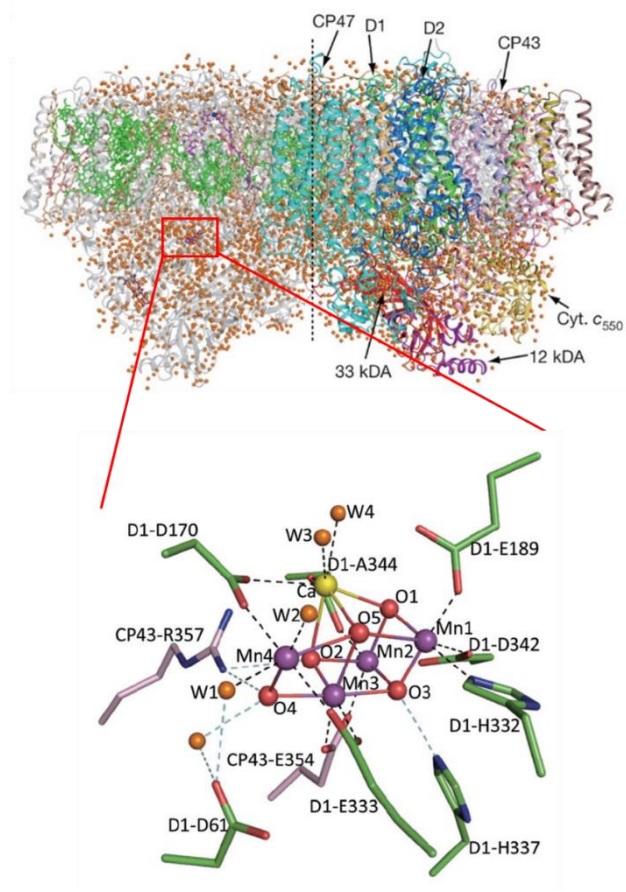


Figure 1.3 Overall structure of PS II at a resolution of 1.9 Å and structure of OEC involving the Mn_4Ca cluster and surrounding proteins.

1.3.3 Hydrogen-bond network and protein channel in PS II

Hydrogen-bond networks in second shell protein around OEC (Figure 1.4) is important because they play a key role in transporting substrate water, protons and release O₂ out of OEC.²² There are a lot of voids between protein structure in PS II, and these were proposed as water and O₂ channels. However, it was revealed that most of these voids are impermeable to water having energy barrier of ~22 kcal/mol in water transport through molecular dynamic.²³

These day, only three possible water channels were reported as shown in Figure 1.5. The Asp61 channel, also called narrow channel, is connected from D1-Asp61 to the O4 bridge of the Mn₄Ca cluster with hydrogen-bonds. The W1 ligand of Mn4 is regarded as associated with this channel, and Pantazis, Cox and co-workers reported that water molecules are inserted to Mn4 in S₂-S₃ transition.^{22,24} On the other side of D1-Asp61, another channel passes the vicinity of Mn4 and proximal Cl⁻, so called Cl⁻ channel or broad channel. Proton is transferred through this channel in deprotonation step in S₂-S₃ transition. In this step, D1-Asp61 acts as the proton acceptor. Last channel is Ca²⁺ channel, also known as large channel, involving Ca bound water (W3, W4) and vicinity of the O1 bridge. Considering these site of OEC has hydrophobic nature and Ca²⁺ may facilitate the release of O₂ molecules, Ca²⁺ channel is proposed to be responsible for O₂ release as well as water substrate delivery.²³ Calculated energy barriers for water transport are 9 kcal/mol, 12 kcal/mol

and 10 kcal/mol for each channel.

Through H/D or ^{18}O isotope experiments and protein mutant experiments, the role of hydrogen-bond networks in water channels is reported to be important in water substrate exchange. According to H/D isotope experiments, the rate of exchange of two water substrate is highly reduced, which means that hydrogen bonding is important for the movement of water molecules.²⁵ However, the degree of rate reduction is different between two water substrate, which means that two water molecules are transported by different mechanisms or by different channels. The importance of hydrogen-bond networks was also reported through protein mutant experiments. PS II containing mutation of amino acid residue belonging to the water channels shows slow kinetics for water exchange. In mutation of D1-Asp61N that Aspartic acid (Asp) amino acid in D1 protein exchanged to asparagine (Asn), water exchange rate is slow down by 3 and 6.5 times,²⁶ respectively, which means hydrogen-bond networks contribute to water oxidation kinetics critically.

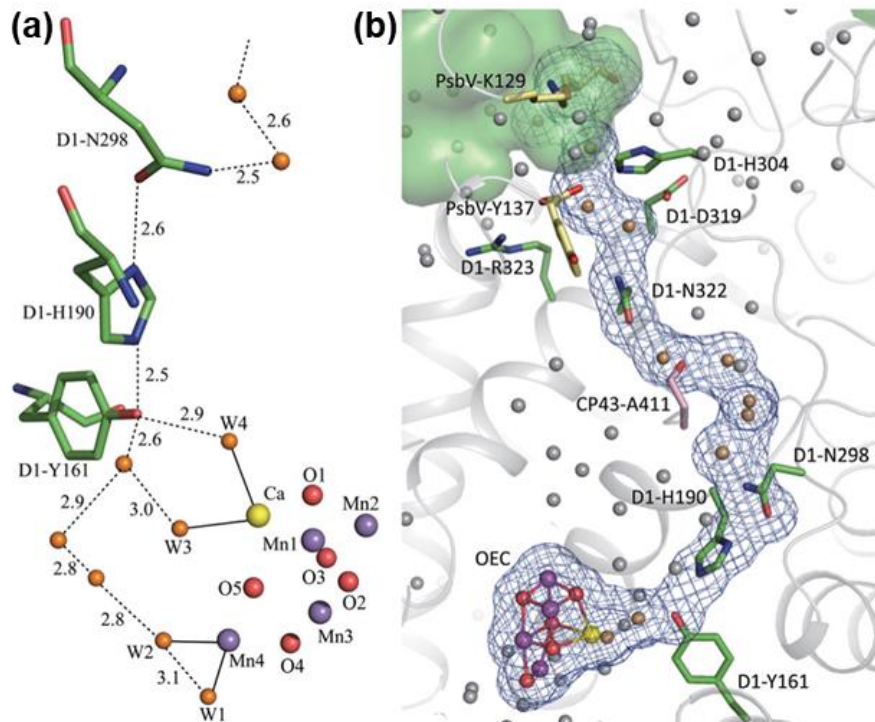


Figure 1.4 Hydrogen-bond networks surrounding OEC. (a) H-bond around Yz. Solid line depicts the bond between metal and water molecules, and H-bonds are represented as dashed lines. (b) H-bond networks from Mn4Ca cluster to luminal bulk phase.

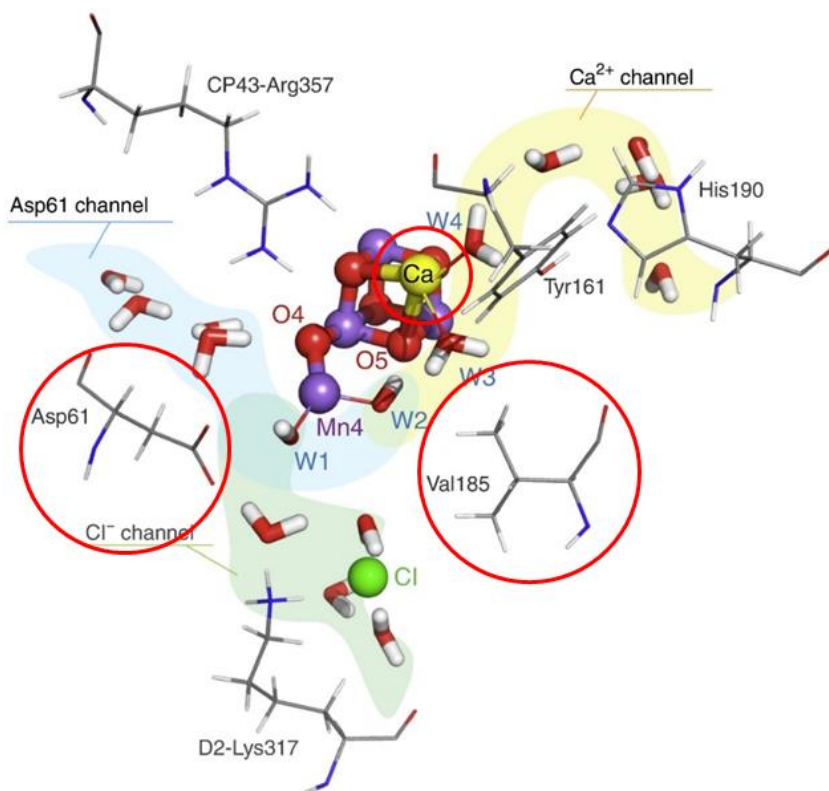


Figure 1.5 Proposed water channels and surrounding amino-acid residues. Circled Asp61, Val185 and Ca²⁺ in Mn₄Ca cluster play central roles to make entropic contribution favorable.

1.3.4 Entropic contribution to water oxidation in PS II

Distorted cubane structure of Mn_4Ca cluster and hydrogen-bond networks surrounding the cluster are characteristics of biological catalyst which have superior catalytic performance for oxygen evolving compared with artificial catalysts. In order to mimic Mn_4Ca cluster and its performance, fundamental challenge is to understand the catalytic mechanism specifically and investigate the roles of atomic components and coordinated amino-acid residue. Although it is hard to probe intermediates, especially in $S_3 - S_0$ transition, due to the too short halftimes of these state, development of time-resolved techniques gives some clues in understanding mechanism. Also, through mutant PS II where specific site was exchanged, the roles of components on the catalytic activities have been revealed. According to these studies, it has been known that OEC has an entropy-favorable structural and mechanistic characteristic.

The Kok cycle for water oxidation and Gibbs free energy of formation intermediate are shown in Figure 1.6.²⁷ Dau and co-worker monitored redox state and structural change in metal centers of Mn_4Ca cluster in real time with 10-ms resolution through time-resolved X-ray absorption spectroscopy (XAS).²⁷ In this study, they found that S_4 state was formed without changing oxidation state of Mn and Y_z. They also showed that Gibbs energy of S_4 formation is pH dependent and affected by H_2O/D_2O isotope exchange. Considering these findings, they reported that

ambiguous S_4 state is formed by deprotonation reaction before O-O bond formation. Importantly, formation of S_4 state is entropy-driven ($\Delta G = -0.1$ eV, $\Delta H = +0.1$ eV, $-T\Delta S = -0.2$ eV), which supports the proton release into the bulk-phase water.

In the absence of mechanistic understanding about $S_3 - S_0$ state, Ca^{2+} in the Mn_4Ca cluster, D1-Asp61, and D1-Val185 in second shell proteins are revealed to contribute reaction kinetics severely by mutation experiments. As shown in Figure 1.7, mutant PS II which contains i) Ca^{2+} was exchanged to Sr^{2+} (Sr-PS II), ii) Asp in D1-Asp61 was exchanged to Asn (D1-D61N), and iii) Val in D1-Val185 was exchanged to Asn (D1-V185N) exhibits slow kinetics of oxygen evolving after injecting third flash. Reaction mechanism for $S_3 - S_0$ transition is presented in Figure 1.7. After proton release during the $S_3^+Y_z^* \rightarrow S_3Y_z^*$ transition, O-O bond is formed and dioxygen is released from cluster. For the Sr-PS II, D1-D61N and D1-V185N, half time of both lag phase and slow phase got longer than wild type PS II (WT-PS II). Through the temperature dependent kinetic studies, Baussac and co-workers reported that Sr-PS II showed highly unfavorable activation entropy ($T\Delta^\ddagger S$) for both phases, while enthalpy of activation ($\Delta^\ddagger H$) for both phases were similar with WT-PS II.²⁵ Considering Ca/Sr exchange hardly affects the structure of Mn_4Ca cluster in the S_0 , S_1 , S_2 and S_3 states, and the Ca/Sr has similar enthalpies for water dissociation whereas Sr has significantly lower entropic term than Ca, they insisted Ca^{2+} determines the entropic contribution in $S_3 - S_0$ transition associated with reorientation of water molecule bound to Ca. Furthermore, Nilsson et al. suggested that highly ordered intermediate could be formed in WT-PS II before O-O bond

formation step compared to Sr-PS II, which supported the favorable entropic contribution of Ca-PS II.²⁸ In addition to Ca ion, it was revealed that D1-Asp61 and D1-V185 also play a role to make entropy favorable. Burnap and co-worker reported that the kinetic slowdown of mutant PS II (D1-D61N and D1-V175N) stemmed from highly negative entropy of activation.²¹ Mutants PS II could not form the optimal configuration at transition state, so required high entropic energy barrier. Because Asp and Val are associated with water and proton channels and they suggested these negative entropies may be attribute to the impeded reorganization of OEC during water exchange or deprotonation step.

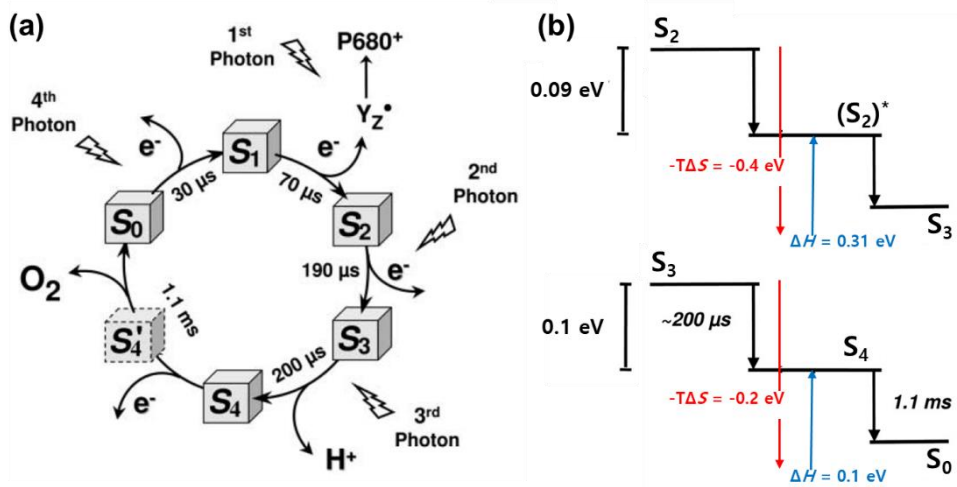


Figure 1.6 The entropic contribution in formation of intermediate species during $S_2 - S_3$, and $S_3 - S_0$ transition. (a) The kok cycle of photosynthetic oxygen evolution. (b) Energetic schemes for $S_2 - S_3$, and $S_3 - S_0$ transition.

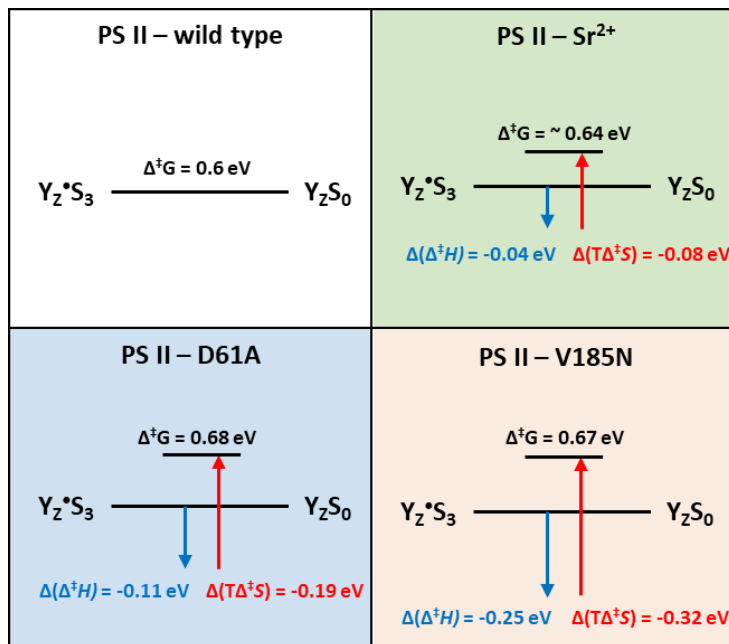


Figure 1.7 Increase of energy barrier for mutant PSII due to the unfavorable entropic contribution. Substitution of Ca²⁺ to Sr²⁺ induces the decrease activation entropy (TΔ[‡]S) by disturbing the formation of ordered transition state prior to O-O bond formation. Two amino-acid residues (Asp61 and Val185) consist of water channel, and substitution of Asp to Asn (D61A) and Val to Asn (V185N) also induce the decrease of TΔ[‡]S.

1.4 Enzyme Catalysis in Nature

In nature, all of the various biochemical reactions which occur in biological system including animals, plants, and microorganisms are regulated by enzymes. Enzymes are the catalysts that lower the activation energy barrier of reactions, thereby crucially enhance the rate of reactions in mild condition of cells. They are composed of proteins or catalytic RNA. Comparing with the classical artificial catalysts, enzymes have several advantages. First, reaction kinetics with enzymes is much faster than with catalysts, even in the mild reaction condition of temperature, pressure, pH, or electric potential. Moreover, enzyme reaction shows high selectivity, because each enzymes has their specific substrate for binding. Through this binding site, reaction rate also can be controlled by inhibitor that impede the binding between substrates and enzymes.

For development of the highly active and selective catalyst, fundamental challenges are identifying the key factors which contribute to the enzyme kinetics and mechanism. Here, we discuss about the origins of fast kinetics based on the entropic contribution in enzyme reaction.

1.4.1 Favorable entropic contribution of enzyme catalysis

The origin of the fast kinetics in the enzymatic reaction has long been a major interest in chemical society, and was found to be associated with favorable activation entropy ($T\Delta^\ddagger S$) by several causes.²⁹ Figure 1.8 shows the free energy diagram for enzyme reaction and importance of entropic contribution is represented in Table 1.1. At first, it was reported that enzyme – substrate (E-S) binding makes entropic contribution ($T\Delta^\ddagger S$) favorable to reaction kinetics, because vibrational entropy needed to overcome transition state may already be paid when substrates are frozen by enzymes.³⁰ This hypothesis, known as Circe effect, has been supported by lots of experimental results. Wolfenden and co-workers showed that ribosome needs near zero entropy of activation ($\Delta^\ddagger S$) for peptide bond formation reaction that is at least 13 kcal/mol lower than for the reaction in water.³¹ These favorable entropic contribution is sufficient to account for the $2 * 10^7$ -fold rate enhancement in ribosome catalysis

Besides the enzyme-substrate binding effect, it was proposed that hydrogen-bond network or pre-organized protein channels surrounding active site stabilize the activated complexes in transition state.^{34,35} In recent calculation study, it was reported that entropic cost for solvent reorganization was reduced in ribosome by hydrogen bond network.³² Also, Chen and co-workers reported that E₃ ligase confers a large entropic effect to lower the energy barrier in protein modification.³³ From the

experimental measurement, favorable activation entropy but unfavorable activation enthalpy was also observed. Based on molecular dynamic simulation, it was revealed that a number of bound water molecules were stabilized within the E3 ligase which results in favorable activation entropy during liberating water molecules at transition state.

In case of deamination of cytidine³⁶ and hydrolysis of guanosine triphosphate (GTP)³⁷, in which both activation enthalpy and entropy are reduced by enzyme (Table 1.1), the origin of entropic contribution was proposed to change of reaction mechanisms with lower activation entropy. As a result of computational calculation for both reaction, it was reported that OH⁻ attack mechanism could be involved on the enzyme reaction which intrinsically shows positive $T\Delta^\ddagger S$, different with non-enzyme reaction. The charged intermediate states such as OH⁻ can be stabilized in electrostatically pre-organized enzyme, and the speed of mechanism can be highly accelerated with positive entropic contribution.

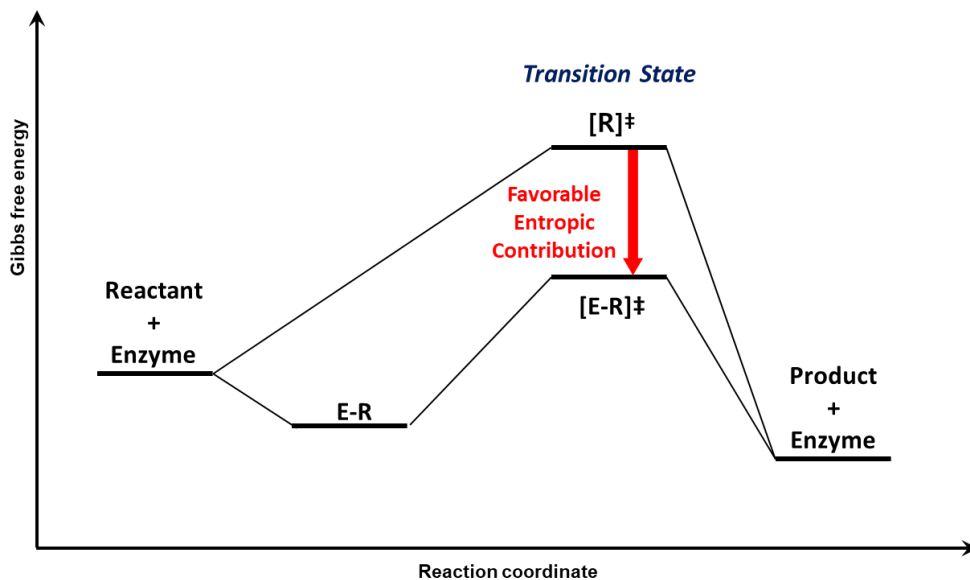


Figure 1.8 Scheme which represents the entropic contribution in enzyme reaction. Favorable entropic contribution in enzyme reaction has been explained by two theories. First, required entropic energy barrier decrease due to the loss of vibrational entropy of substrate during the enzyme-substrate binding. In addition, transition state could be stabilized in enzyme by H-bond networks or pre-organized surrounding proteins.

Enzyme	Reaction		$\Delta^\ddagger G$ (kcal/mol)	$\Delta^\ddagger H$ (kcal/mol)	$-T\Delta^\ddagger S$ (kcal/mol)
Ribosome	Peptide formation	W	14	16	-2
		W/O	22.2	9.1	13.1
E3 Ligase	Protein modification	W	11	24	-12.9
		W/O	15	10.7	4.3
Cytidine deaminase	Cytidine deamination	W	14	14.9	-0.9
		W/O	30.4	22.1	8.3
EF-Tu	GTP hydrolysis	W	14.2	21	-7
		W/O	27.9	25	2.8

W : Reaction condition with enzyme

W/O : Reaction condition without enzyme

Table 1.1 Measured activation energetic parameters for various enzyme reaction. Gibbs energy of activation ($\Delta^\ddagger G$) decreased by enzyme, and measured $\Delta^\ddagger H$ and $\Delta^\ddagger S$ showed it was derived from entropic contribution, not enthalpic contribution.

1.5 Artificial Electrocatalysts for Water Oxidation

1.5.1 Bioinspired Mn based Catalyst

There has been an attempt to synthesize efficient catalysts by applying lessons from the biological enzyme systems. In nature Photosystem II, oxygen evolving center (OEC) efficiently catalyze the OER under neutral condition with markedly higher turnover frequency. The OEC consists of an inorganic Mn_4CaO_5 cluster and its unique ligand environment (Figure 1.3). From the recent X-ray analysis, detailed structural information of Mn_4CaO_5 cluster was obtained.²⁰ The cluster has low-symmetry structure containing a distorted cubane core of Mn_3CaO_4 with fourth Mn bridged through one oxygen of the cubane core. This Mn_4CaO_5 cluster undergoes successive changes in oxidation state and its geometry, taking part in a so-called Kok cycle (Figure 1.6).

One key lesson we could get from the biological system is that the distorted structure plays an important role in the stabilization of high valent Mn oxidation state and catalytic activity. For example, Driess group developed amorphous MnO_x nanoparticles whose local structure and oxidation state of Mn are similar to Mn_4CaO_5 cluster.³⁸ Amorphized MnO_x nanoparticles showed higher catalytic activity. Moreover, Dismukes group made $\lambda\text{-MnO}_2$ by removing Li ions from LiMn_2O_4 , which structure is similar with that of Mn_3CaO_4 core of the cluster.³⁹ Interestingly, $\lambda\text{-MnO}_2$ showed catalytic activity whereas the parent LiMn_2O_4 was inactive.

Improved OER activity was also reported from Dau group by switching the voltage during the electrodeposition. From X-ray adsorption spectroscopy (XAS) analysis, they found active catalyst had a disordered Mn geometry and mix oxidation state of Mn (III/IV).⁴⁰ In addition, many manganese-based heterogeneous OER catalysts have been reported inspired by the unique properties of OEC. In an effort to translate the principles of the biological OEC to synthetic heterogeneous manganese-oxide-based catalysts, our group also synthesized several manganese-based heterogeneous catalysts such as hydrated manganese (II) phosphate⁴¹, lithium manganese pyrophosphate⁴², and manganese oxide nanoparticles⁴³. Through a series of experiments, we found that the stabilization of Mn (III) by the distorted geometric structure plays an important role in the OER activity. It has been shown that the lessons from biological Mn_4CaO_5 cluster can be successfully applied to synthetic heterogeneous OER electrocatalysts.

1.5.2 Computational entropic consideration in DFT study

In previous section, importance of entropic contribution was represented in biological water oxidation in PS II and various enzyme catalysis. Here, we explain how entropy is considered in synthetic catalysis. Computational results are suggested in this chapter, and experimental results will be summarized in next chapter.

In computational studies, the change in entropy (ΔS) is calculated using DFT calculations of the vibrational frequencies and standard tables for gas phase molecules. Calculated entropy of H₂O and H₂ molecules and reaction intermediates are summarized in Table 1.2.^{7, 10, 44-47} Entropy of H₂O and H₂ are considered from the thermodynamic data base, and in case of intermediate species, vibration entropy is mainly calculated or approximated to 0.

Considering these calculation results, we represented the entropy energy diagram within different O-O bonding formation mechanism in Figure. 1.9. In both radical coupling mechanism (RC mechanism) and acid-base mechanism (AB mechanism), entropy (S) increase in deprotonation step while one proton is released to bulk solution. After that, during O-O bond formation, there is severe difference in entropic contribution between two mechanisms. In RC mechanism, additional entropic energy barrier was not required in RDS where two oxo radicals form O-O bond. On the other hand, in AB mechanism, huge entropic energy is needed to form O-O bond. This is because during O-O bond formation by nucleophilic attack of water molecule, the degree of freedom of whole system highly decrease as much as the vibrational, rotational, and translational entropy of water molecule. As shown in Figure 1.9, entropic contribution ($T\Delta^\ddagger S$) for AB mechanism was calculated to -0.48 eV, while RC mechanism has positive entropic contribution, $T\Delta^\ddagger S = + 0.19$ eV.

	Cubic ABO ₃	Co ₃ O ₄	N-doped graphene	Na ₂ CoP ₂ O ₇	RuO ₂	MO
H ₂ O	0.66	0.67	0.67	0.67	0.22	0.67
H ₂	0.4	0.4	0.41	0.4	0.4	0.41
*O	0.05	0.05	0.05	0	0	0
*OH	0.08	0.06	0.07	0	0	0
*OOH	0.14	0.14	0.16	0	0	0
OO					0	
Ref	<i>PCCP</i> 20 (2018)	<i>ACS Catal.</i> 6 (2016)	<i>J. Catal.</i> 314 (2014)	<i>Nat. Commun.</i> 6 (2015)	<i>JACS</i> 132 (2010)	<i>JPCC</i> 118 (2014)

 Thermodynamic data base
 Calculation of vibration entropy

Table 1.2 Reported TS (eV) from the DFT study for various materials (T=25°C).

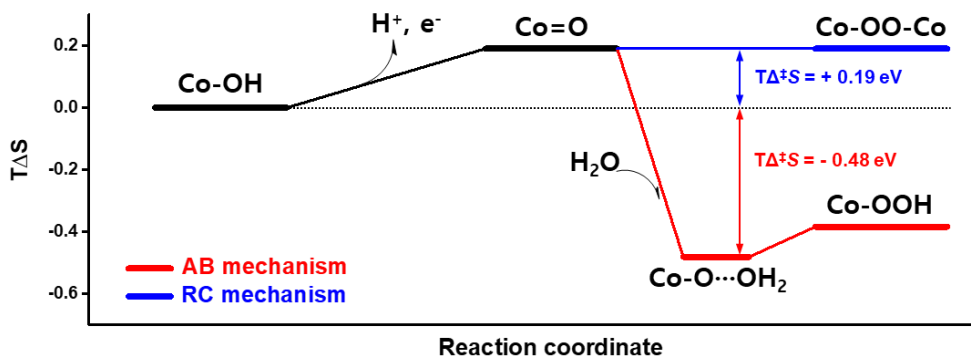


Figure 2.9 $T\Delta S$ diagram based on the DFT calculation. Co-OH is initial state and Co=O is formed by deprotonation step. After that, O-O bond formation step is following through acid-base mechanism (AB mechanism) and radical coupling mechanism (RC mechanism). RC mechanism has positive entropic contribution due to the deprotonation step. On the other hand, highly negative activation entropy ($T\Delta^\ddagger S$) is required in nucleophilic attack of H₂O in O-O bond formation (T=25°C).

1.5.3 Experimental measurement of entropy

Temperature dependent analysis to measure kinetic barrier have also been conducted in electrochemical heterogeneous and homogeneous catalysis. As shown in Table 1.3, in homogenous system, Gibbs energy of activation ($\Delta^\ddagger G$) can be measured by $\Delta^\ddagger H$ and $\Delta^\ddagger S$. Moreover, reaction mechanisms can be also understood based on the entropic contribution to reaction kinetics. According to recent reports, highly negative entropic contribution ($T\Delta^\ddagger S = -0.61$ eV at 25°C) was observed in O-O bond formation by nucleophilic attack of water molecules, while there was little entropic contribution in intermolecular O-O bond formation.

In contrast to molecular catalysis, in which detailed understanding has already been established, both description of activity trends and OER mechanism for heterogeneous system has not been yet fully validated based on experimental results. In heterogeneous system, only activation energy (E_a), which is converted to activation enthalpy ($\Delta^\ddagger H$) by $E_a = \Delta^\ddagger H + RT$, has been measured and reported, due to the difficulties of measuring activation entropy ($\Delta^\ddagger S$). Although some reports tried to evaluate catalytic performance or identify OER mechanism based on activation enthalpy, these approaches had fundamental limitation that entropic contribution was excluded in estimating kinetic barrier ($\Delta^\ddagger G = \Delta^\ddagger H - T\Delta^\ddagger S$). Therefore, without considering activation entropy, temperature dependent analysis is not necessarily able to unravel the precise nature of reaction kinetic and mechanism.

System	Reaction	Catalyst	$\Delta^\ddagger H$ (eV)	$T\Delta^\ddagger S$ (eV)	Ref
Heterogeneous	OER	NiFeO _x	0.24 ($\eta = 0$)		48
		Ni	0.75 ($\eta = 0$)		49
		FeCo	0.62 ($\eta = 0.3$ V)		50
		NiFeOOH	0.68 ($\eta = 0$ V)		51
		NiCo ₂ O ₄	0.72 ($\eta = 0$)	Not reported	52
	ORR	Pt	0.38 ($\eta = 525$)		53
		Pt-Fe	0.4 ($\eta = 525$)		54
	HER	Pt	0.08 ($\eta = 0$)		55
CER	RuO ₂	0.91 ($\eta = 0$)		56	
Homogeneous	OER	K ₂ FeO ₄	0.11	-0.003	57
		Cp*Ir(2,2-bpy) ₂ Cl	0.17	-0.11	58
		Cp*Ir ^{III} (NHC)Cl ₂	0.18	-0.03	59
	Ru ^V =O → Ru ^{III} -OOH in OER	Ru ^{II} (bpc)(bpy)OH ₂	0.18	-0.61	60
	Olefin oxidation (O-O bond cleavage)	[Fe ^{II} (TPA)(NCCH ₃) ₂] ²⁺	0.47	-0.29	61
		[(TMC)Fe ^{III} -OOH] ²⁺	0.58	-0.23	62

Table 1.3 Measured activation parameters ($\Delta^\ddagger H$ and $\Delta^\ddagger S$) through temperature dependent kinetic analysis in heterogeneous and homogeneous catalyst systems (*T = 25°C).

1.5.4 Transition state theory for electrochemical OER

In 1935, Henry Eyring developed the Eyring equation to describe the chemical reaction rate dependent on temperature based on transition state theory.⁶³

$$k = \frac{k_B T}{h} \exp\left(\frac{-\Delta^\ddagger G}{RT}\right)$$

In this equation, rate constant (k) is determined by Gibbs energy of activation ($\Delta^\ddagger G$) which is the energy barrier of reaction. In the chemical reaction, $\Delta^\ddagger G$ cannot be controlled unless the reaction or enzyme is changed.

However, in an electrochemical reaction, the energy barrier can be controlled by the electrode potential because the electrochemical potential (μ) of the reactant on the electrode can increase or decrease with the electrode potential. Therefore, the reaction kinetics of an electrochemical half-reaction can be described as follows. The location of the transition state is defined as the symmetric factor (β), and η is $E - E_0$.

$$k_+ = \frac{k_B T}{h} \exp\left(\frac{-(\Delta^\ddagger G^0 - \beta \eta F)}{RT}\right)$$

When a reaction is composed of multi-step electron transfer steps, the reaction kinetics depends on two factors.

- i) Potential dependent energy barrier of electron transfer reaction in the rate-determining step (RDS). It is affected by the symmetric factor (β) that is usually 0.5 for an electron transfer reaction, 0 for a chemical reaction.

- ii) Potential dependent population of reactant in RDS which means equilibrium state of pre-RDS steps is changed by electrode potential. Equilibrium state of electrochemical reaction is governed by Nernst equation.

$$E = E_0 - \frac{RT}{F} \ln\left(\frac{a_{Red}}{a_{Ox}}\right)$$

Considering these two factor, reaction rate of multi-electron transfer reaction is described as below.

$$k_+ = \frac{k_B T}{h} \exp\left(\frac{-(\Delta^\ddagger G^0 - \alpha E F)}{RT}\right)$$

$$\alpha = n_p + n_q \beta$$

α is transfer coefficient where n_q is the number of electrons transferred in RDS, and n_p is the number of electrons transferred prior to RDS. This equation is so-called Butler-Volmer equation.⁶⁴

The free energy diagram of electrochemical oxygen evolution reaction is represented in Figure 1.10. In this diagram, reaction mechanism was considered to typical OER mechanism with 4 electron transfer steps and O-O bond formation as rate determined step (RDS). Initial state of electrode was assumed to M-OH, based on the previous reports for mechanistic studies in neutral condition.⁴ To consider the kinetic energy barrier, free energy of transition state (TS) of RDS was depicted. The reaction rate of OER is determined by kinetic energy barrier which is difference of

energy level between initial state (M-OH) and TS with highest free energy.

Under standard electrode potential (E°), reaction has kinetic energy barrier as high as standard Gibbs energy of activation ($\Delta^\ddagger G^\circ$), and it decrease gradually in proportion to transfer coefficient (α) as applying overpotential (η). In multi-step electron transfer reaction, transfer coefficient of oxidation reaction is defined as below (1) when n_p is the number of electrons transferred prior to RDS, n_q is the number of electrons transferred in RDS, and β is symmetric factor for RDS. And, the electrochemical reaction rate is expressed by the Butler-Volmer equation (2). $\Delta^\ddagger G^\circ - \alpha F \eta$ represents the potential dependence of Gibbs energy of activation, and Γ_{act} is the number of active site.

$$\alpha = n_p + n_q \beta \quad (1)$$

$$i = nF \frac{k_B T}{h} \Gamma_{act} \exp\left(\frac{-\Delta^\ddagger G^\circ}{RT}\right) \exp\left(\frac{\alpha F \eta}{RT}\right) \quad (2)$$

Several kinetic parameters can be measured based on the temperature dependent kinetics of the Butler-Volmer equation (3). In the Eyring plot as shown in Figure 1.11, the linear slope and y-intercept have kinetic meaning related to $\Delta^\ddagger H$ and $\Delta^\ddagger S$. As described in (4), potential dependent activation enthalpy ($\Delta^\ddagger H$) could be measured in Eyring plot, and the slope of Eyring plot gradually decrease with increasing overpotential ($\eta_1 < \eta_2$).

$$\ln\left(\frac{i}{T}\right) = -\frac{\Delta^\ddagger H^\circ}{RT} + \frac{\alpha F \eta}{RT} + \frac{\Delta^\ddagger S}{R} + \ln\left(nF \frac{k_B}{h} \Gamma_{act}\right) \quad (3)$$

$$slope = \frac{\Delta^\ddagger H^\circ - \alpha F \eta}{R} = \frac{\Delta^\ddagger H}{R} \quad (4)$$

$$y - intercept = \frac{\Delta^\ddagger S}{R} + \ln \left(nF \frac{k_B}{h} \Gamma_{act} \right) \quad (5)$$

However, several kinetics parameters such as the number of active site (Γ_{act}) or Gibbs energy of activation ($\Delta^\ddagger G$) should be known, in order to obtain the activation entropy through (5) or (6). In molecular catalysis where most of catalytic centers are dispersed in electrolyte, evaluation of Γ_{act} or $\Delta^\ddagger G$ is straightforward. However, the presence of a non-active bulk phase in heterogeneous catalysts makes the investigation of kinetic parameters (Γ_{act} or $\Delta^\ddagger G$) challenging, which result in hardness of measuring activation entropy ($\Delta^\ddagger S$) experimentally.

$$\Delta^\ddagger G = \Delta^\ddagger H - T\Delta^\ddagger S \quad (6)$$

Recently, Bard group proposed the methodology to measure the rate constant (k) and the number of active site (Γ_{act}) for heterogeneous electrochemical reaction via surface interrogation scanning electrochemical microscopy (SI-SECM). In this paper, kinetic parameters for Co-Pi was investigated and it was reported that 11 Co site/nm² are involved as active site in Co-Pi film, and rate constant for OER as 1.2 s⁻¹ - 3.2 s⁻¹ at 0.41 V overpotential. Gibbs energy of activation ($\Delta^\ddagger G$) can be calculated to 0.75 eV - 0.73 eV based on Eyring equation (7). From these advanced time-resolved surface titration method, it become possible to measure the activation entropy of Co-Pi film in heterogeneous OER. In this paper, based on the reported two kinetic parameters for Co-Pi (k , Γ_{act}), we calculated the entropy of activation

($\Delta^\ddagger S$) for OER on Co-Pi through temperature dependent analysis.

$$k = \frac{k_B T}{h} \exp\left(\frac{-\Delta^\ddagger G}{RT}\right) \quad (7)$$

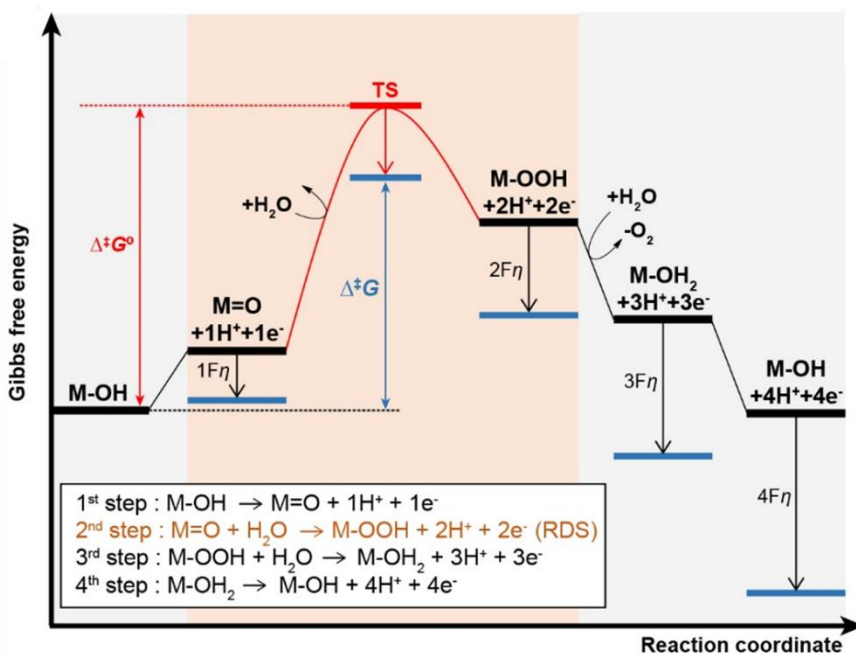


Figure 1.10 Free energy diagram of typical electrochemical oxygen evolution reaction. It is assumed that reaction is proceeded by acid-base mechanism, and O-O bond formation step is rate determining step (RDS). The experimentally measured activation parameters are the difference of energy state between initial state and transition state of RDS. Red bar and black bars represent the free energy of activated species in RDS, and free energy of intermediate species at standard electrode potential (E°), respectively. Blue bars represent the free energy of intermediates when overpotential (η) is applied.

1.6 Objective of the Thesis

For the decades, people tried to develop the OER catalysts with characteristics close to PS II having TOF around 50 O₂ molecules per second at 60 mV overpotential. However, k_0 of iridium oxide, which is reported to have the best properties among the artificial catalysts, is far below that PS II.⁶⁵ Considering these novel metal based catalysts such as iridium oxide or ruthenium oxide are located near the top of the volcano plot, breakthrough other than the previously reported descriptor, which is based on the enthalpic contribution, is needed.

Indeed, the superior kinetic of enzymes in nature, including PS II, is contributed from the entropic effect. From now on, many researchers reported the activation energy parameters in molecular catalysis through temperature dependent kinetic analysis. In heterogeneous electrochemical reaction, however, only few studies reported activation energy or enthalpy of activation, not activation entropy as shown in Table 1.3. These are result from the difficulties to measured temperature dependent kinetics for electrochemical reaction and to identify the number of active sites in heterogeneous reaction.

In this study, we have attempted to investigate the entropic contribution in heterogeneous electrochemical water oxidation reaction. Using temperature dependent Eyring plot, we successfully measured the kinetic energy barrier containing enthalpy and entropy of activation for Mn₃O₄ nanoparticles and Co-Pi

films. As a result, we confirmed that activation entropy contributes highly unfavorable to reaction kinetics. Based on the reported calculation entropy value, the origin of entropy effect was proposed to mechanistic effect that nucleophilic attack of water molecules during O-O bond formation.

$$i = nF \frac{k_B T}{h} \Gamma_{act} \exp\left(\frac{-\Delta^\ddagger G^0}{RT}\right) \exp\left(\frac{\alpha F \eta}{RT}\right)$$

$$\ln\left(\frac{i}{T}\right) = -\frac{\Delta^\ddagger H^0}{RT} + \frac{\alpha \eta F}{RT} + \frac{\Delta^\ddagger S}{R} + \ln\left(nF \frac{k_B}{h} \Gamma_{act}\right)$$

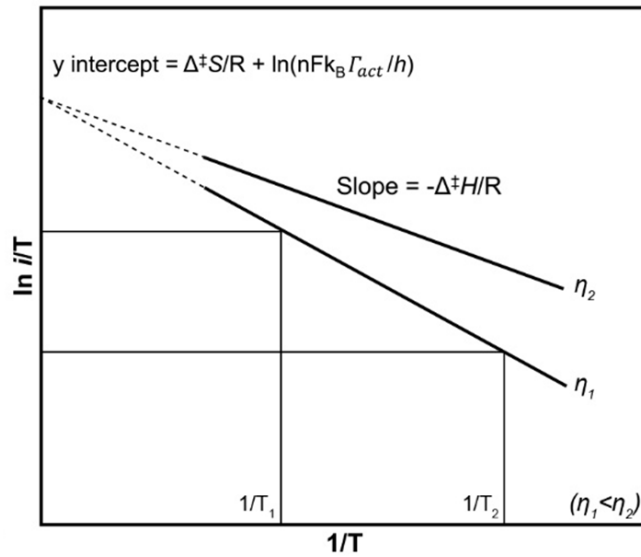


Figure 1.11 Butler-Volmer equation and Eyring plot for electrochemical reaction.

($\Delta^\ddagger G$: Gibbs free energy of activation, $\Delta^\ddagger H$: enthalpy of activation, $\Delta^\ddagger S$: entropy of activation, α : transfer coefficient and Γ_{act} : the number of active site).

	Arrhenius model	Eyring model
Kinetic equation	$k = Ae^{-E_a/RT}$	$k = \frac{k_B T}{h} e^{\Delta^\ddagger S/R} e^{-\Delta^\ddagger H/RT}$
	$\frac{\partial(\ln k)}{\partial T} = \frac{E_a}{RT^2}$	$\frac{\partial(\ln k)}{\partial T} = \frac{\Delta^\ddagger H + RT}{RT^2}$
Plot	$\ln i \text{ vs. } \frac{1}{T}$	$\ln \frac{i}{T} \text{ vs. } \frac{1}{T}$
Slope	$-\frac{E_a}{R}$	$-\frac{\Delta^\ddagger H}{R}$
Y-intercept	$\ln nF\Gamma_{act}A$	$-\frac{\Delta^\ddagger S}{R} + \ln\left(\frac{nFk_B\Gamma_{act}}{h}\right)$

Table 1.4 Comparison of kinetic equation and energetic parameters which can be measured from temperature dependent analysis between Arrhenius and Eyring model.

Chapter 2. Experimental and Procedure

2.1 Preparation of catalysts

2.1.1 Materials

Manganese acetate dehydrate ($\text{Mn}(\text{CH}_3\text{COO})_3 \cdot 2\text{H}_2\text{O}$, 97%), Myristic acid ($\text{CH}_3(\text{CH}_2)_{12}\text{COOH}$, $\geq 99\%$), Octadecene ($\text{CH}_3(\text{CH}_2)_{15}\text{CH}=\text{CH}_2$, 90%), $\text{K}_2\text{Ir}(\text{IV})\text{Cl}_6$ (99.99%), $\text{Na}_2\text{HPO}_4 \cdot 7\text{H}_2\text{O}$ (ACS reagent, 98.0-102.0%) and $\text{NaH}_2\text{PO}_4 \cdot 2\text{H}_2\text{O}$ (99.0%) were purchased from Sigma Aldrich and $\text{Co}(\text{NO}_3)_2 \cdot 6\text{H}_2\text{O}$ (ACS, 98.0-102.0%) was purchased from Alfa Aesar. Decanol ($\text{CH}_3(\text{CH}_2)_9\text{OH}$, $\geq 99\%$) was purchased from Tokyo Chemical Industry (TCI) and Toluene ($\text{C}_6\text{H}_5\text{CH}_3$, 99.5%) and Acetone (CH_3COCH_3 , 99.5%) were purchased from Daejung Chemical and Metals. All chemicals were used without additional purification. Fluorine doped Tin-Oxide coated glass (FTO, TEC-8) which has $15\Omega/\text{sq}$ surface resistivity was obtained as precut by $1.0\text{ cm} \times 1.5\text{ cm}$ glass pieces from Pilkington Company.

2.1.2 Manganese oxide nanoparticles (Mn₃O₄ NPs)

The manganese oxides nanoparticles were synthesized via hot injection method to obtain ~10 nm mono-disperse sphere nanocrystals.⁴³ 1 mmol of manganese acetate dehydrate (Mn(CH₃COO)₃·2H₂O), 2 mmol of myristic acid, and 20 ml of octadecane were mixed and heated up to 110 °C under continuous degassing for 90 min. 3 mmol of decanol was mixed with 1 mL of octadecene to form a solution and this solution was heated at 110 °C under degassing for 90 min with vigorous stirring at another glass pot. After 90 min, the temperature of manganese precursor was raised to 295 °C under Ar atmosphere and then the mixture of decanol was injected rapidly for the fast nucleation. The color of the solution changed into dark brown from brown at 110 °C and pale yellow at 295 °C after hot injection. The temperature of the mixed solution was maintained at 285 °C for 1 hour and sequentially the mixture was cooled down to room temperature. The synthesized manganese oxide nanoparticles were washed with toluene and acetone with centrifugation at 13500 RPM for 2 min. The washing process was conducted 3 times. Washed nanoparticles were dispersed in hexane solution and spin coated onto FTO glass.

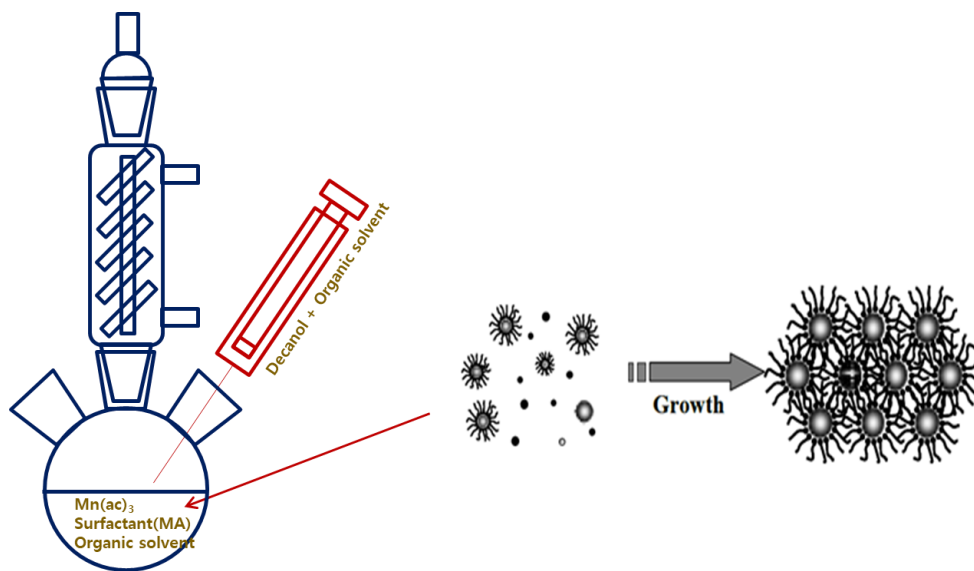


Figure 2.1 Scheme for synthesizing manganese oxide nanoparticles by hot injection method.

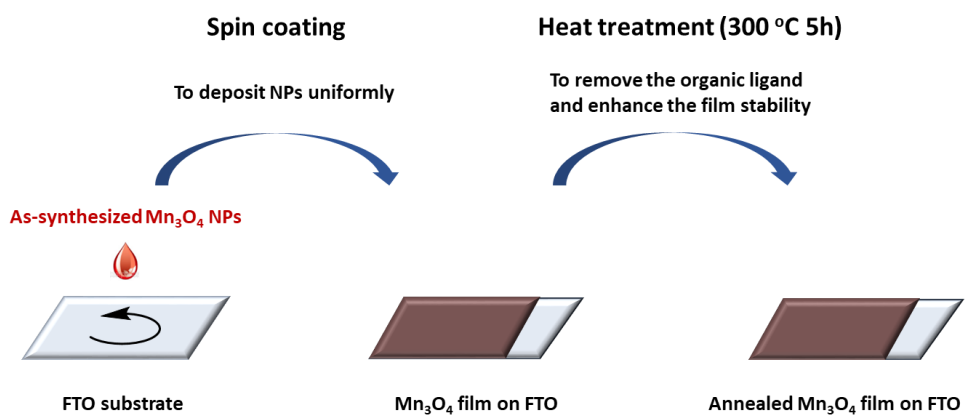


Figure 2.2 Scheme for preparing manganese oxide nanoparticles film.

2.1.3 Cobalt phosphate (Co-Pi)

Catalyst films were prepared via controlled potential electrolysis of 0.1 M potassium phosphate (KPi), pH 7.0 electrolyte solutions containing 0.5 mM Co^{2+} . To minimize precipitation of cobalt phosphate, 25 mL of 0.2 M KPi was added to 25 mL of 1.0 mM Co^{2+} solution. The solutions thus prepared remained clear over the course of all depositions. Depositions were carried out using a FTO glass as the working electrode. Deposition by controlled potential electrolysis was carried out on quiescent solutions at 1.047 V vs. NHE without iR compensation. A typical deposition lasted 30 min for a 10 mC/cm² film. Following deposition, films were rinsed thoroughly in deionized water to remove any adventitious Co^{2+} and Pi.

2.2 Characterization

2.2.1 Powder X-ray diffraction (XRD)

Powder X-ray diffraction (XRD) was carried out on a New D-8 Advance X-ray diffractometer with Cu K α radiation ($\lambda=1.54056\text{\AA}$). For the measurement, manganese oxide nanoparticles were centrifuged and precipitated powder was annealed at 300 °C during 5 hours. The powder was loaded on Si holder, retrofitted in X-ray diffractometer. XRD patterns were recorded in a range of 10 ~ 80° with a step of 0.02° and a velocity of 0.02°/8 s. Obtained XRD patterns were compared with previously reported JDPDS cards.

2.2.2 Scanning electron microscopy (SEM)

The morphology of catalysts on FTO glass was characterized with a high resolution scanning electron microscope (Supra 55VP, Carl Zeiss, Germany). SEM sample for Mn₃O₄ nanoparticles, and Co-Pi were prepared using previously mentioned method as film state.

2.2.3 Transmission electron microscopy (TEM)

Transmission electron microscopy (TEM) images and selected area electron diffraction (SAED) patterns were obtained using a high resolution transmission electron microscope (2100F, JEOL, Japan) with an acceleration voltage of 200 kV. TEM samples were prepared via two different ways. For the Mn_3O_4 nanoparticles, hexane solution containing Mn_3O_4 nanoparticles was dropped on the TEM grid and dried in an oven.

2.3 Electrochemical Methods

2.3.1 Cyclic voltammetry (CV) measurements

All electrochemical experiments were conducted under a three-electrode electrochemical cell system. A BASi Ag/AgCl/KCl 3M reference electrode and a Pt foil (2 cm × 2 cm × 0.1 mm, 99.997% purity, Alfa Aesar) were used as a reference electrode and a counter electrode, respectively. Electrochemical tests were carried out at ambient temperature using a potentiostat system (VSP 300, Bio-Logic Science Instruments). Electrode potential was converted to the NHE scale, using the following equation: $E(\text{NHE}) = E(\text{Ag}/\text{AgCl}) + 0.210 \text{ V}$. Additionally, overpotential values were calculated by the difference between the iR corrected potential ($V = V_{\text{applied}} - iR$) and the thermodynamic point of water oxidation at a specified pH. The electrolyte was phosphate buffer with 500mM buffer strength under the pH 7. The electrolyte was stirred vigorously during the measurement to prevent the mass transport problem.

2.3.2 Tafel slope analysis

Tafel slope analysis was conducted to investigate how electrons are

transferred in electrochemical reaction for Mn₃O₄, and Co-Pi. In order to measure the potential step to achieve 10 fold of faradaic current density, we measured current density at applied potential using chronoamperometry (CA, VSP 300, Bio-Logic Science Instruments), because charging current effect could be ignored. Starting potential was determined to the point where the current begins to increase from charging current range, and the measurement was completed at a potential of about 5 mA/cm². Potential steps were about 10 mV in the measuring range. The stabilized current was measured during 30 seconds, and average value in this range was calculated as the faradaic current at each potential. After plotting the current density in log scale (Log j/Acm⁻²) vs. applied potential, tafel slope was measured via linear fitting from 10⁻⁴ A/cm² to 10⁻³ A/cm² from below equation. The α in the equation is transfer coefficient for reaction.

$$\text{Tafel slope} = \left(\frac{\partial E}{\partial \log j} \right)_{pH} = \frac{2.3 RT}{\alpha F}$$

2.3.3 Temperature dependent electrochemical measurements

As explained in introduction part, activation energy parameters can be measured via temperature dependence of reaction kinetics. In order to measure the reaction rate that equal to current density in electrochemical reaction at applied

potential, we set up the temperature dependent analysis system. First, we prepared the reversible hydrogen electrode (RHE) as reference electrode. By using RHE, potential of working electrode can be accurately controlled without any effect on the temperature dependence of the reference electrode. Furthermore, in order to use RHE in neutral pH electrolyte without liquid junction potential, we used RHE where hydrogen gas contacts the electrolyte solution directly through gas diffusion Pt/Pd electrode (HydroFlex RHE, Gaskatel) as shown in Figure 2.3. In this system, we successfully measured temperature dependent kinetics of electrochemical reaction from 20°C to 70°C via CV measurement and CA measurement. All experiments were conducted under stirring condition to prevent mass transport effect.

2.3.4 Electrochemical active surface area (ECSA)

Electrochemical capacitance was determined using cyclic voltammetry (CV) measurements. The potential range where there is a non-Faradaic current response was determined from CV. This range is typically a 0.1 V window centered at OCP of the system. CV measurements were conducted in quiescent solution by sweeping the potential across the non-Faradaic region from the more positive to more negative potential and back at 8 different scan rates: 0.005, 0.01, 0.025, 0.05, 0.1, 0.2, 0.4, and 0.8 V/s. The working electrode was held at each potential vertex for 10 s before

beginning the next sweep. Measured charging current (i_c) is equal to the product of the electrochemical double layer capacitance (C_{DL}) and the scan rate (v) as shown in eq 1.

$$i_c = vC_{DL}$$

Plotting i_c as a function of v yields a straight line with slope equal to C_{DL} . The electrochemically active surface area (ECSA) of the catalyst can be calculated by dividing C_{DL} by the specific capacitance of the sample as shown in eq 2.

$$ECSA = C_{DL}/C_s$$

Here we use a general specific capacitance of 0.040 mF/cm².

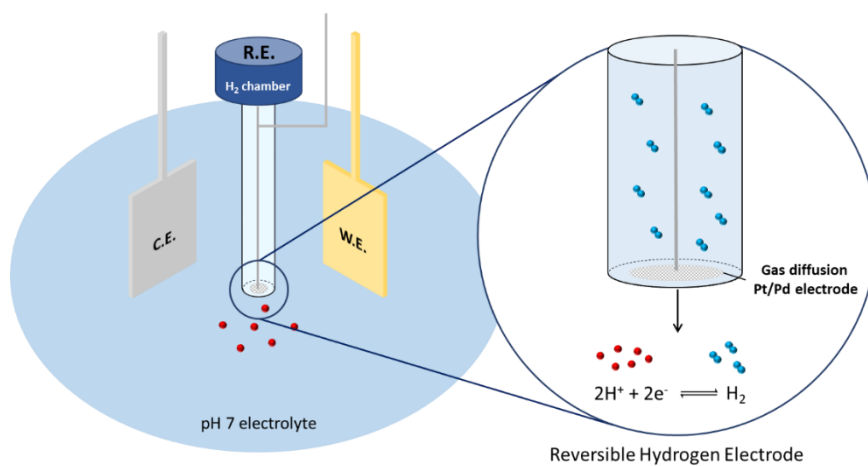
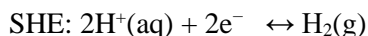
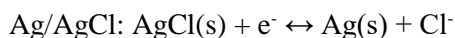
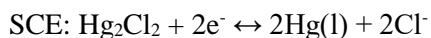


Figure 2.3 Scheme for methodology to control W.E. versus RHE in neutral condition. In gas/electrolyte interface, we can directly measure W.E. vs. RHE without liquid junction potential.

Chapter 3. Results and Discussion

3.1 3.1 Set-up the Electrochemical Cell

In order to control the working electrode in higher temperature, we used reversible hydrogen electrode (RHE) which independent on the temperature. This is because, in case of other reference electrode, the electrode potential of half reaction depends on the temperature, resulting in the difficulty of controlling working electrode.



When using the liquid based RHE, the liquid junction potential, which is derived from the pH gradient between neutral electrolyte and RHE containing acidic solution, makes it difficult to measure the working electrode potential (Figure 3.1a). Therefore, to remove liquid junction potential in the system, we used gas diffusion hydrogen electrode that hydrogen gases are supplied from H₂ cartridge and diffused to electrolyte through permeable Pt electrode. To ensure that the hydrogen electrode operate well in our system, we measured electrode potential of Ag/AgCl (KCl 3M)

versus RHE from acidic condition to neutral condition. As a result, Figure 3.1b shows Ag/AgCl (KCl 3M) was precisely measured in pH range. The slope 0.059 is pH dependence of RHE and electrode potential of Ag/AgCl (KCl 3M) is 0.21 V.

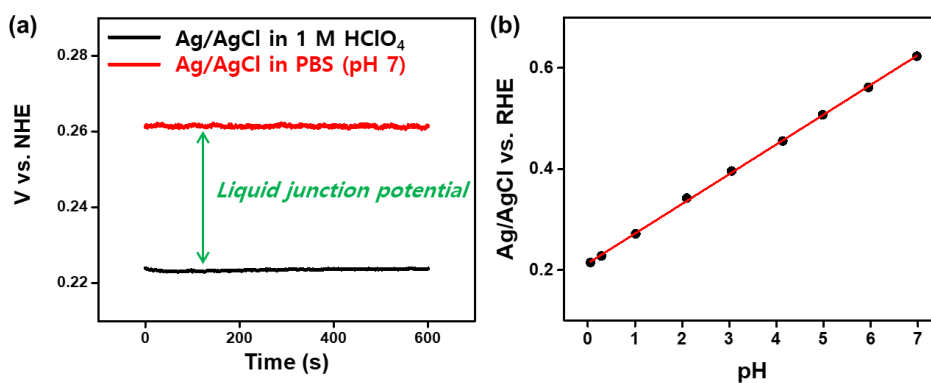


Figure 3.1 (a) Liquid junction potential in acidic solution based R.H.E system. (b) Validation of hydrogen electrode system in neutral condition. Ag/AgCl (KCl 3M) electrode was used as working electrode and gas diffusion RHE was used as reference electrode. Every points were measured by open circuit potential measurement.

3.2 Characterization of Catalyst

3.2.1 Manganese oxide nanoparticles (Mn_3O_4 NPs)

We synthesized manganese oxide nanoparticles via conventional hot injection method. The TEM image shows uniformed 8 nm size nanoparticles were synthesized (Figure 3.3). After annealing under 300°C during 5 hours, phase of manganese oxide nanoparticles was confirmed as Mn_3O_4 (Figure 3.2) from XRD pattern and PDF cards. As shown from SEM analysis (Figure 3.3), monodisperse 8 nm sized Mn_3O_4 nanoparticles were successfully loaded onto the FTO substrates via spincoating method. The thickness of the Mn_3O_4 nanoparticles films was about 230 nm.

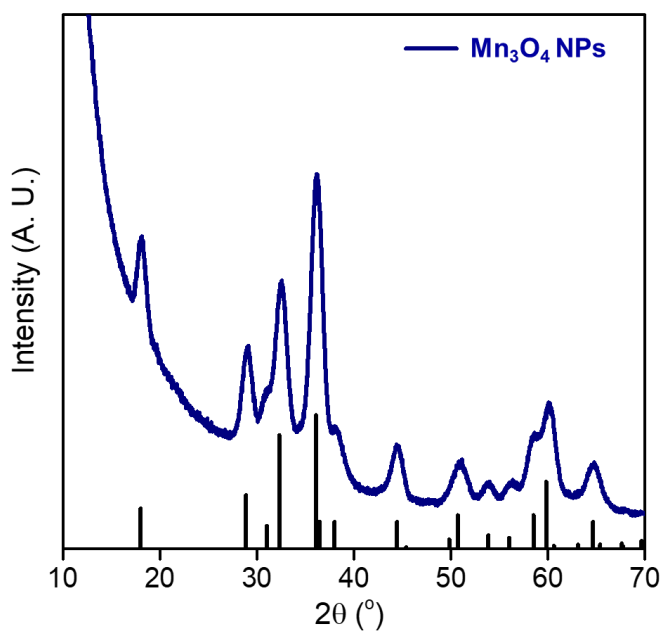


Figure 3.2. The XRD pattern of powder Mn₃O₄ NPs. Black bar represents the reference PDF card of Mn₃O₄ (PDF #: 00-024-0734).

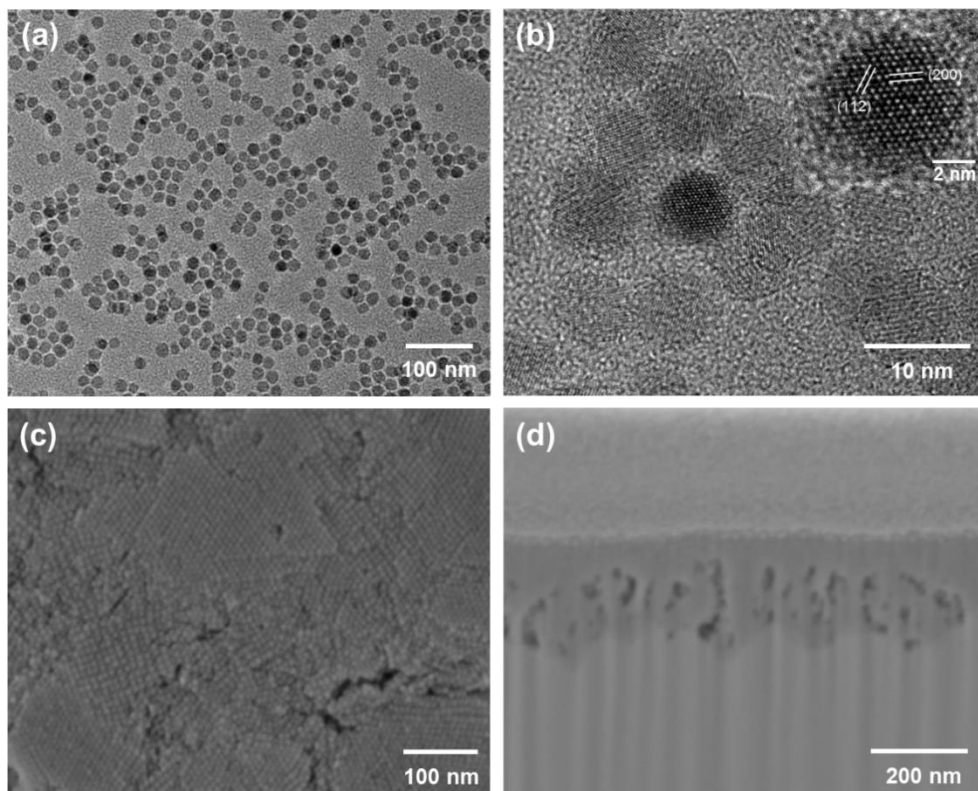


Figure 3.3. Electron microscopic images of Mn_3O_4 NP. (a-b) TEM image of synthesized Mn_3O_4 NPs. Inset of (b) shows a high resolution image of the Mn_3O_4 crystal. (c-d) Plane and cross sectional SEM images of Mn_3O_4 NPs films on FTO substrates.

3.2.2 Cobalt phosphate (Co-Pi)

In previous reports, the phase of cobalt phosphate was conformed as crystalline Co_3O_4 forming amorphous overlayers film by high-resolution transmission electron microscopy (HRTEM).⁶⁶ As shown in Figure 3.4, we successfully synthesized the cobalt phosphate catalyst film deposited onto the FTO substrate. And SEM image and SEM-EDS histogram conformed that micro sized amorphous cobalt oxide particles were coated uniformly on the FTO.

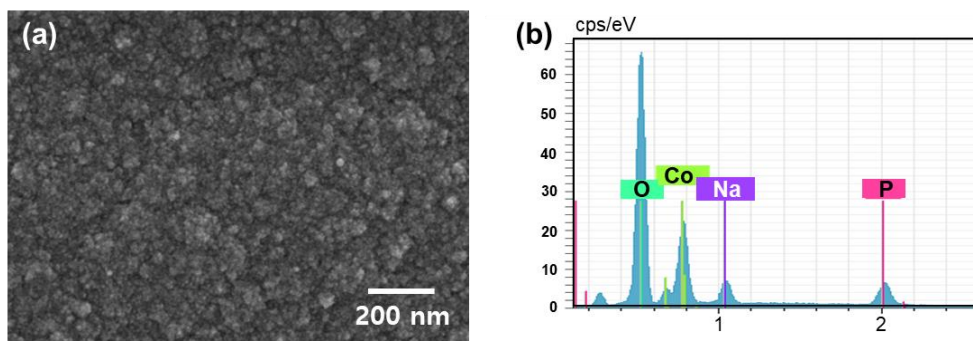


Figure 3.4 Characterization of Co-Pi films by SEM (a) Plane SEM image for Co-Pi film. (b) SEM-EDS histogram for deposited Co-Pi film.

3.3 Electrochemical Characterization

The catalytic activities of three electrocatalysts were characterized by CV measurement and Tafel analysis. CV curves were measured at phosphate buffer, pH 7, and presented to polarization curve eliminating charging current effect. Comparing the catalytic activities in Figure 3.5a, Mn_3O_4 nanoparticles and Co-Pi showed similar performance for OER. The overpotential at 10 mA/cm^2 was measured to 540 mV and 560 mV, respectively.

The Tafel slope is important parameter for not only catalytic activities, but also mechanistic information. The measured Tafel slope was shown in Figure 3.5b. For the Co-Pi, previous reports by Nocera group proposed Tafel slope of Co-Pi was 60 mV/dec meaning transfer coefficient is 1⁴. In mechanistic aspect, this value means Co-Pi has chemical RDS and one electron is transferred before the RDS step. In the result from our Tafel analysis, Co-Pi showed about 70 mV/dec that was similar value with reported one. Also, for the Mn_3O_4 nanoparticles, Nam group reported Tafel slope of Mn_3O_4 nanoparticles as ~80 mV/dec.⁵ In the reported paper, transfer coefficient was estimated to 1, and large value was explained as result from the limiting factors such as charge transport resistance. In our result, Mn_3O_4 nanoparticles also showed 75 mV/dec that is slightly lower value that reported one. This may result from the difference in method measuring the Tafel slope. In our analysis, we measured Tafel slope via CA method to eliminate charging current

effect or redox current effect, where CV method was used in previous report. In the mechanistic aspect, Mn_3O_4 nanoparticles also contained chemical RDS with 1 electron transfer step in pre-RDS.

For catalysis of Mn_3O_4 NPs and Co-Pi, RDS is suggested to O-O bond formation step. Through the in-situ spectroscopy analysis, such as in-situ UV, XANES, and Raman, Nam group proposed that the sequential oxidation of Mn(II,III,IV) generate Mn(IV)=O species and O-O bond formation step is followed as RDS.⁵ Also, Nocera group suggested that after concerted one proton and one electron transfer step while Co(III) is oxidized to Co(IV), chemical O-O bond formation is followed.⁴

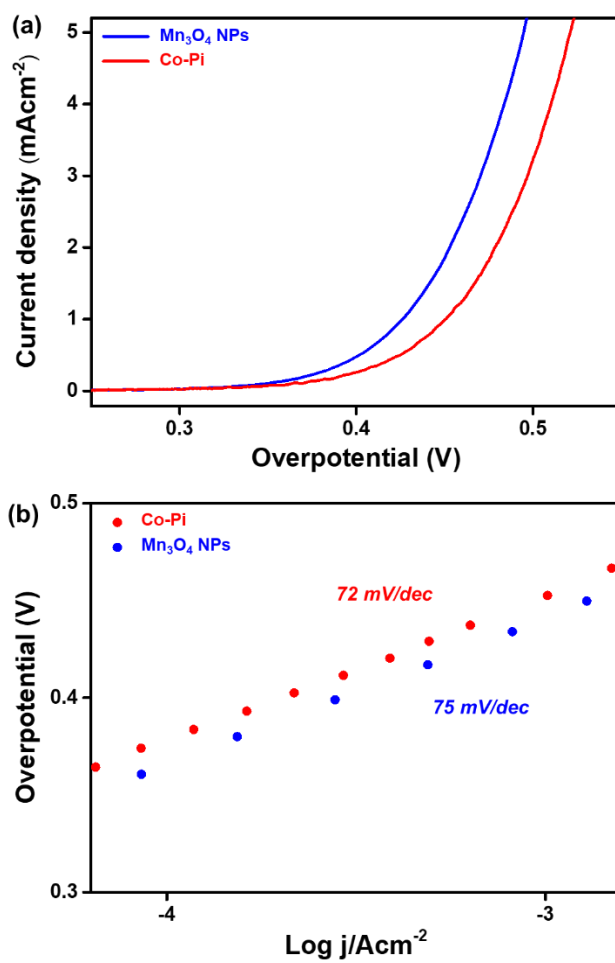


Figure 3.5 Electrokinetic characterization of Mn₃O₄ NPs and Co-Pi. (a) Polarization curve and (b) Tafel slope in neutral condition (pH 7).

3.4 Investigation of Entropic Contribution

3.4.1 Temperature dependent kinetic analysis

Temperature dependent kinetics of catalysts was characterized from 20 °C to 70 °C. Figure 3.6 represents the polarization curve of Mn₃O₄ nanoparticles, and Co-Pi. As expected, the kinetics of catalysis was increased gradually with increasing temperature. Below equation represents temperature dependent current density in Tafel region, where Γ_{act} is active site for catalysis.

$$i = nF\Gamma_{act} \frac{k_B T}{h} \exp\left(\frac{-(\Delta^\ddagger G^0 - \alpha EF)}{RT}\right)$$

Through these temperature dependency, we tried to measure activation energy parameters in next section.

The Tafel slope was also measured from 20 °C to 70 °C in order to investigate whether the mechanism of OER changes within temperature. As a result, the Tafel slopes were measured in similar range within temperature, which means the mechanisms of catalysts was not changed by increasing temperature. As shown in Table 3.1, Tafel slope slightly decrease in higher temperature, which would be caused by change of α as previously reported. Considering that all of Tafel slope were in range of 60 mV/dec, we confirmed that catalysis was proceeded by same mechanism in which 1 electron was transferred prior to chemical RDS.

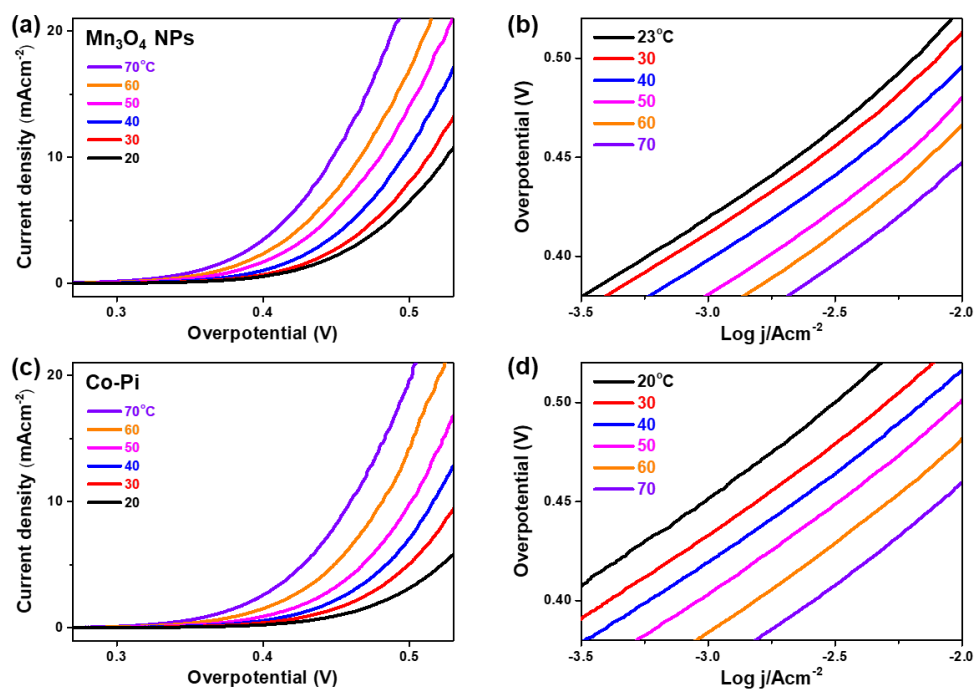


Figure 3.6 Temperature dependent kinetics of OER. Polarization curves (a) and Tafel slope (b) of Mn₃O₄ NPs, and (c, d) Co-Pi.

Temperature	Tafel slope (mV/dec)	
	Mn₃O₄ NPs	Co-Pi
20 °C	79	86
30 °C	77	83
40 °C	76	80
50 °C	75	79
60 °C	74	76
70 °C	74	73

Table 3.1 Temperature dependent Tafel slope of Mn₃O₄ NPs, and Co-Pi.

3.4.1.1 Analysis on the enthalpy of activation ($\Delta^\ddagger H$)

The enthalpy of activation ($\Delta^\ddagger H$) was measured by temperature dependent kinetic analysis based on the Eyring equation.⁵⁶ As explained at introduction, the slope of Eyring plot means the enthalpy of activation ($\Delta^\ddagger H$). In Figure 3.7, Eyring plots at various potential were shown for Mn₃O₄ nanoparticles, and Co-Pi. At each potential, Log (j/T) have linear relation with inverse temperature. From the slope of each linear relation, we can measure the enthalpy of activation with potential successfully. The measured values were plotted with overpotential in Figure 3.8. The enthalpy of activation ($\Delta^\ddagger H$) decreased linearly as potential increase. This relation is well matched with theoretical Butler-Volmer equation as below.

$$\Delta^\ddagger H^0 - \alpha EF = \Delta^\ddagger H$$

From this equation, the transfer coefficient (α) can be measured from the slope of $\Delta^\ddagger H$ vs. overpotential. In this result, α of Mn₃O₄ NPs, and Co-Pi were measured to 0.74, and 0.96 respectively. In order to verify our temperature dependent analysis, we compared measured α with previously reported value which was measured by Tafel slope analysis. From the Tafel slope analysis, α of Mn₃O₄ NPs was measured to 0.78 based on the Figure 3.5b. In case of Co-Pi, α was reported to 1 in previously reported paper. These results are highly comparable with our analysis results, meaning that our temperature dependent analysis system well reflect

electrochemical kinetics of OER catalysis.

As a results, through temperature dependent analysis, we can successfully measure the enthalpy of activation ($\Delta^\ddagger H$) for Mn_3O_4 NPs and Co-Pi. As measuring the $\Delta^\ddagger H$ at low overpotential region, we confirmed that energy barrier linearly decreased with applied potential. Based on Butler-Volmer equation, the slope of linear line represent transfer coefficient (α) and we verified the reliability of our analysis by comparing the measured α with the results from Tafel slope analysis.

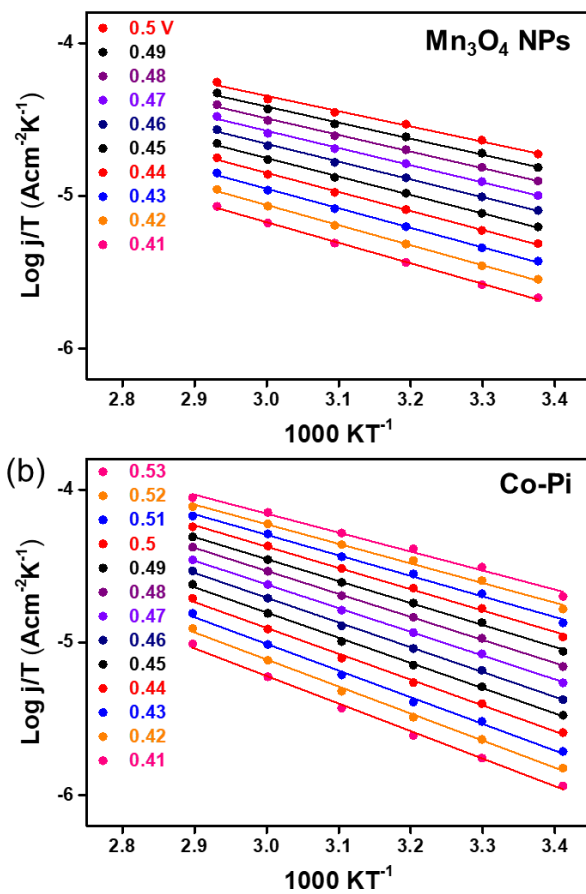


Figure 3.7 Eyring plot for (a) Mn_3O_4 NPs, and (b) Co-Pi from 20°C to 70°C.

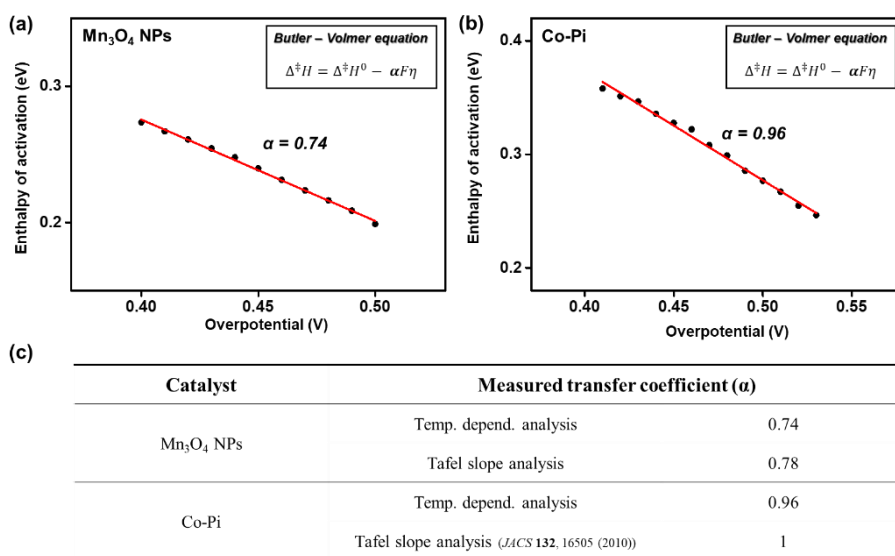


Figure 3.8 Confirmation of measured transfer coefficient (α). Potential dependent enthalpy of activation ($\Delta^\ddagger H$) for (a) Mn₃O₄ NPs, and (b) Co-Pi. α was measured by Butler-Volmer equation. (c) Measured α in our work and Tafel slope analysis. Accordance of α reflect the reliability of these kinetic analysis

3.4.1.2 Analysis on the entropy of activation ($\Delta^\ddagger S$)

In addition to enthalpy of activation ($\Delta^\ddagger H$), entropy of activation ($\Delta^\ddagger S$) was also measured in our work. First of all, $\Delta^\ddagger S$ can be calculated by $\Delta^\ddagger H$ and $\Delta^\ddagger G$ by below equation.

$$\Delta^\ddagger G = \Delta^\ddagger H - T\Delta^\ddagger S$$

Bard and Ahn reported turnover frequency (TOF) of Co-Pi to 1.2/s – 3.2/s at 0.41 V overpotential measured via time-resolved surface titration method^{67,68}, known as surface interrogation scanning electrochemical microscopy (SI-SECM). We can calculate $\Delta^\ddagger G$ at 0.41 V overpotential from TOF through equation between rate constant (k) and $\Delta^\ddagger G$ assuming reverse reaction which is oxygen reduction reaction (ORR) does not occur.

$$k = \frac{k_B T}{h} \exp\left(\frac{-\Delta^\ddagger G}{RT}\right)$$

In our calculation, $\Delta^\ddagger G$ was calculated to 0.73 – 0.75 eV at 410 mV. In addition to $\Delta^\ddagger G$, $\Delta^\ddagger H$ also measured by our work as mentioned in previous section. At 410 mV, $\Delta^\ddagger H$ of Co-Pi was measured 0.35 eV as shown in Figure 3.8. Based on these two parameters, $T\Delta^\ddagger S$ was calculated to -0.4 eV for OER on Co-Pi, suggesting that energy barrier of entropy is quite large considering the $\Delta^\ddagger H$ is 0.35 eV.

In case of Mn_3O_4 NPs, TOF was measured by impedance circuit model

analysis in our group. This research was conducted by H. Seo in our group, and in preparation for research paper. Considering the structure of Mn₃O₄ NPs film, transmission line models was adopted as shown in Figure 3.9a. The parallel R_{int} & C_{int} loops indicated the active sites on the surface of p-MnO NPs. The resistive elements (R_{tr}) with serial connection between RC loops, described electron transport process through assembled p-MnO NPs. Fitted result is shown in Figure 3.9b and it was found that impedance spectra were successfully fitted with our proposed circuit model. In this research, reaction rate constant (*k*) were extracted from the function of R_{int} and C_{int} closely related to surface OER catalysis.

$$k = \frac{1}{R_{int}C_{int}}$$

In the Figure 3.9c, the value of *k* exponentially increased with applied potential, which well mated with Butler-Volmer equation as $k_0 \cdot e^{-\alpha \eta}$. The α can be measured in linear slope and the measured value, which is 0.74, was accord with the results from the temperature dependent analysis and Tafel slope analysis. In this research, rate constant (*k*) of Co-Pi was also measured as shown in Figure 3.9d, and it was comparable with reported values. Through these results, we thought that the measured *k* of Mn₃O₄ NPs is reliable to calculate $\Delta^\ddagger G$.

From the impedance model analysis, rate constant (*k*) were measured to 4.6/s at 0.43 V, and 18.7/s at 0.48 V overpotential. The Gibbs energy of activation ($\Delta^\ddagger G$) was calculated to 0.72 eV, and 0.68 eV, respectively. In our work, enthalpy of activation ($\Delta^\ddagger H$) were measured to 0.25 eV, and 0.22 eV at each potential.

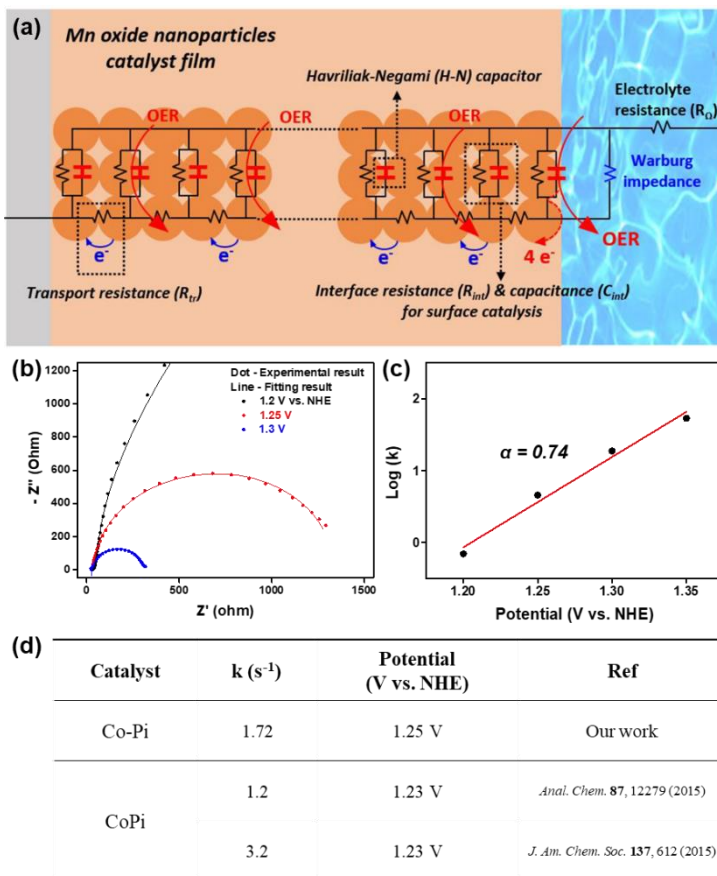


Figure 3.9 (a) Our proposed circuit model for impedance analysis for Mn_3O_4 NPs film. R_{tr} indicate resistance for electron transport in the film. The R_{int} and C_{int} in RC loops, which are described surface catalysis, mean interface resistance and capacitance, respectively. (b) Comparison of rate constant (k) from our model and reported values.

Therefore, $T\Delta^\ddagger S$ was calculated to $-0.46 - 0.47$ eV for Mn_3O_4 NPs catalysis.

To summarize, we calculated $T\Delta^\ddagger S$ for OER catalysis on Mn_3O_4 NPs and Co-Pi. Gibbs energy of activation was calculated from reported TOF of Co-Pi and measured rate constant (k) of Mn_3O_4 NPs. The $T\Delta^\ddagger S$ of Mn_3O_4 NPs was measured to $-0.46 - 0.47$ eV and $T\Delta^\ddagger S$ of Co-Pi was measured to -0.4 eV. In this analysis, the highly negative entropic contribution was observed, and the reason for more contribution of Co-Pi will be discussed later.

Entropy of activation ($T\Delta^\ddagger S$) was also measured through temperature dependent analysis. The y-intercept of Eyring plot contains the information about $T\Delta^\ddagger S$ and the number of active site (Γ_{act}) as below, and we can calculate the $\Delta^\ddagger S$ in our system by calculating Γ_{act} .

$$y \text{ intercept} = -\frac{\Delta^\ddagger S}{R} + \ln\left(\frac{nFk_B\Gamma_{\text{act}}}{h}\right)$$

In order to calculate the Γ_{act} , we tried to postulate the portion of active site on the whole electrode. In Table 3.2, calculated portion of active site in heterogeneous system were represented. The portion of active site was calculated by dividing TOF limit by TOF. TOF limit is assumed TOF value when 100 % of surface metal sites are active. As a result, in heterogeneous system, it is revealed that 0.2 – 0.67 % of whole metal site on electrode are involved in catalytic cycle.

Material	TOF limit (s ⁻¹)	Ref	TOF (s ⁻¹)	Ref	% of Active site
8 nm Mn ₃ O ₄ NPs	0.05 (@η=0.53 V)	<i>Our impedance analysis</i>	22.1 (@η=0.53 V)	<i>Our impedance analysis</i>	0.2 %
5 nm Co ₃ O ₄ NPs	0.02	<i>Nat. Chem.</i> 6 , 365 (2014)	< 3	<i>Nat. Chem.</i> 6 , 365 (2014)	> 0.67 %
Co-Pi	0.002 (@η=0.41 V)	<i>JACS</i> 132 , 16505 (2010)	1.2 (@η=0.41 V)	<i>Anal. Chem.</i> 87 , 12279 (2015)	0.2 %
Material	Coverage	Ref	Active site	Ref	% of Active site
~ 4 nm IrO _x	1.5 mC/cm ²	<i>JPCC</i> 121 , 17873 (2017)	8 μC/cm ²	<i>JPCC</i> 121 , 17873 (2017)	> 0.5 %

TOF limit : TOF value when assuming all surface metal sites (Γ_{max}) are active.

Table 3.2 Reported the number of active site for nano-sized metal oxide catalysts for OER.

To determine electrochemical active surface area (ECSA), double-layer capacitance was measured in Figure 3.10. Cyclic voltammetry were measured in a non-Faradaic region at various scan rate, and double-layer capacitance (C_{DL}) was determined to 5.91 mF by the average of the absolute values of the slope. By dividing the double layer capacitance (C_{DL}) by specific capacitance ($C_s = 0.04 \text{ mF/cm}^2$), ECSA of Mn_3O_4 NPs was calculated to 147.8 cm^2 per 1 cm^2 electrode area. The number of whole metal sites for Mn_3O_4 NPs film was calculated by the following equation with lattice parameter $4.43 \times 10^{-8} \text{ cm}$. As a result, Mn site on the electrode was estimated to $1.5 \times 10^{17} / \text{cm}^2$.

$$(\text{Mn sites}) = (\text{ECSA}) \times (\text{the moles of Mn atoms} / \text{cm}^2)$$

Considering that 0.2 – 0.67 % of metal site are active in heterogeneous system, we assumed that 3×10^{14} (0.2%) – $1 \times 10^{15} / \text{cm}^2$ (0.67%) sites were involved in active site.

In case of Co-Pi, the number of active site (Γ_{act}) for Co-Pi can be calculated based on previously reported active site density of Co-Pi. Active site density of Co-Pi was reported to 11 Co atoms/ nm^2 by Bard and Ahn, which means Γ_{act} is $11 \times 10^{15} / \text{cm}^2$ in neutral condition.⁵⁵

The measured y-intercept for Eyring plot were represented in Figure 3.11. In low overpotential region, y-intercept was uniformly measured, and average value was -1.15 for Mn_3O_4 NPs and 0.18 for Co-Pi. Based on the relation between y-intercept and the number of active site explained above, we can calculate the entropy of activation ($\Delta^\ddagger S$) for both Mn_3O_4 NPs and Co-Pi (Figure 3.12).

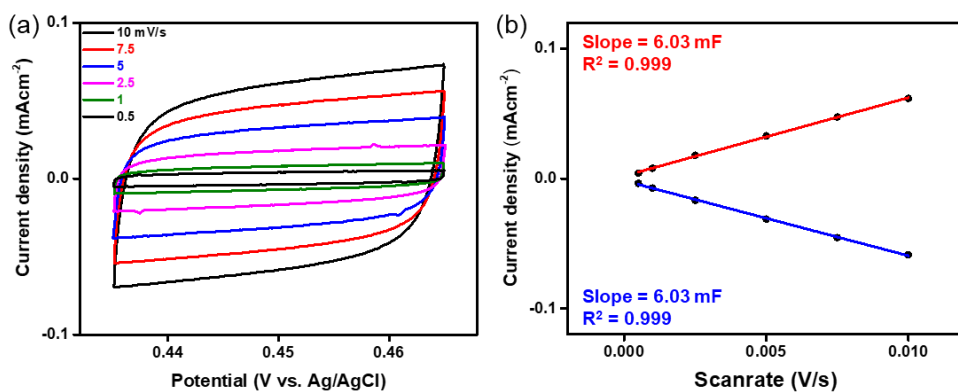


Figure 3.10 Double layer capacitance measurement for determining ECSA analysis for (a, b) Mn₃O₄ NPs. (a) Cyclic voltammograms were measured in a non-Faradaic region at various scan rates. (b) The cathodic and anodic charging currents measured at 0.45 V vs. Ag/AgCl. The determined double-layer capacitance of the system is represented.

Within the $3 \times 10^{14} - 1 \times 10^{15}$ of active sites, $T\Delta^\ddagger S$ for Mn_3O_4 NPs was calculated to 0.46 eV to 0.49 eV, which is highly comparable with $T\Delta^\ddagger S$ from rate constant (k). In case of Co-Pi, $T\Delta^\ddagger S$ was calculated to 0.41 eV, which was significantly equivalent to the value from rate constant (k). Through verifying the measured $T\Delta^\ddagger S$ in two different methods, we confirmed that we successfully measured the activation entropy for OER on the Co-Pi.

From the results for three catalysts, we found that activation entropy works highly unfavorable to reaction kinetics in heterogeneous electrochemical OER. At the overpotential where reaction occurs, entropy of activation ($T\Delta^\ddagger S$) take a huger part of whole energy barrier that enthalpy of activation ($\Delta^\ddagger H$) which has been regarded as crucial kinetic parameter in OER.

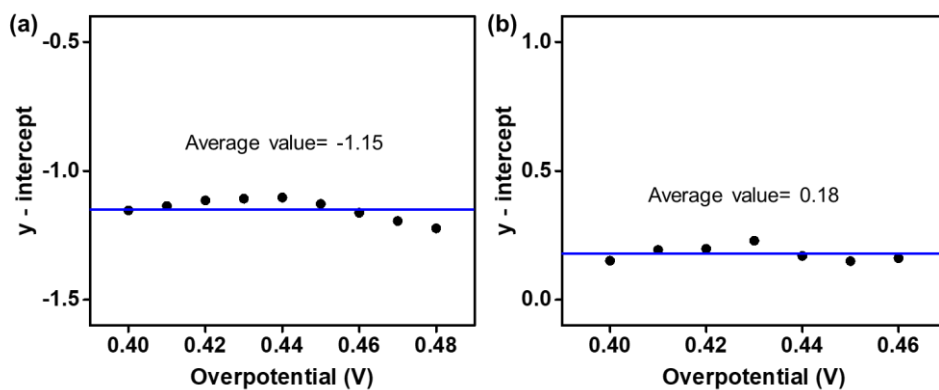


Figure 3.11 Measured y-intercepts in Eyring plot for Mn₃O₄ NPs, and Co-Pi. In low overpotential, y-intercepts were obtained within similar ranges and average value was used in analysis.

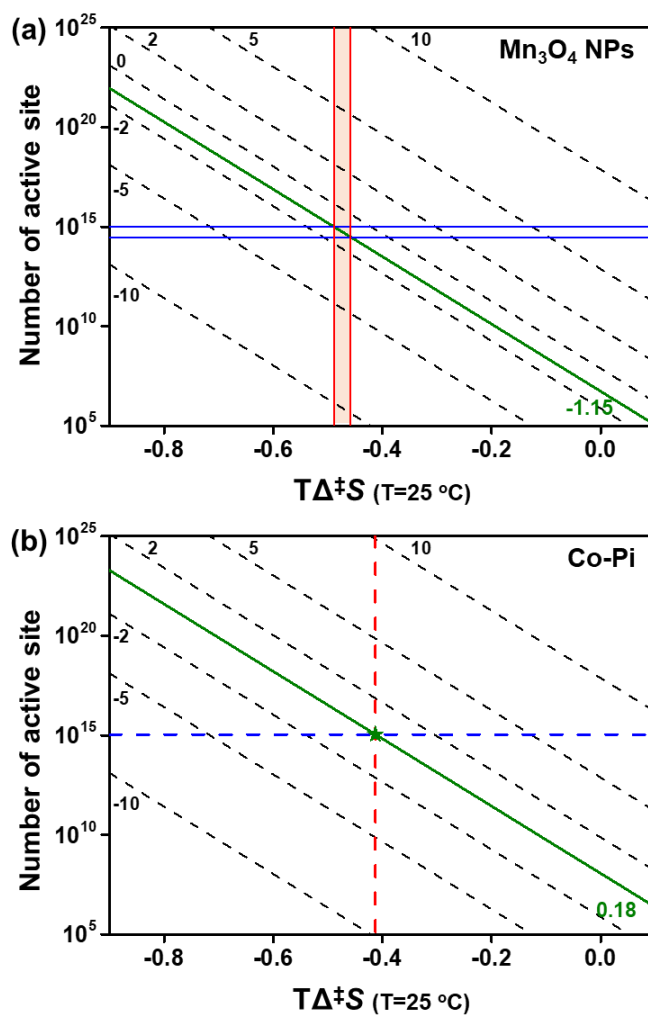
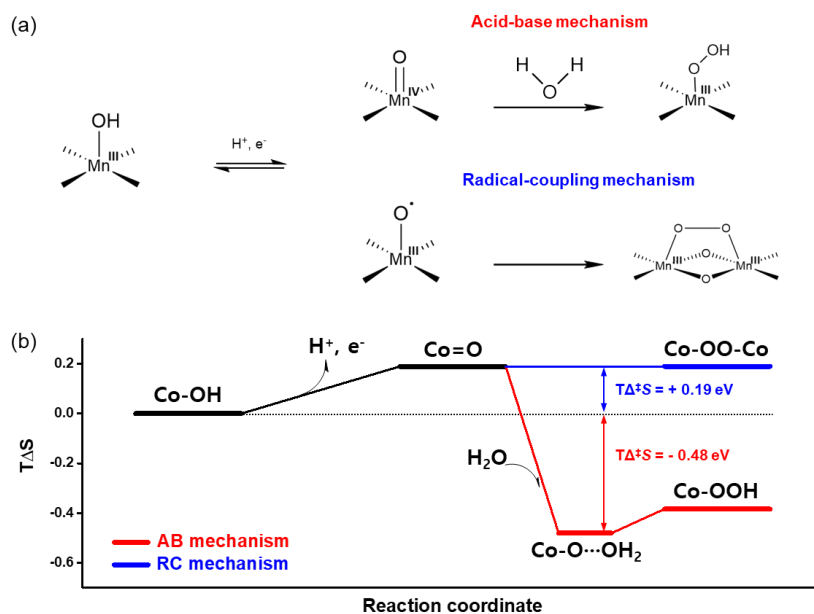


Figure 3.12 Calculated $T\Delta^\ddagger S$ from the temperature dependent analysis for (a) Mn_3O_4 NPs and (b) Co-Pi. Blue line is calculated number of active site (Γ_{act}), and Red line is calculated $T\Delta^\ddagger S$ ($T = 25^\circ\text{C}$).

3.4.2 Entropic contribution to O-O bond formation during water oxidation

Here, based on the reported DFT calculation, we proposed that the highly negative entropy contribution mainly derived from mechanistic effects in O-O bond formation step. In Figure 3.13b, the entropy (TS) diagram is represented for different O-O bond formation mechanism. The entropy values of intermediates species were quoted from the calculated entropy of OER on Co₃O₄ surface. According to the calculation results, entropy (S) increase in deprotonation step in which one proton and electron are released to form Co=O from Co-OH. After that, during O-O bond formation, there is severe difference in entropic contribution between acid-base (AB) and radical-coupling (RC) mechanisms. In RC mechanism, additional entropic energy barrier was not required while two Co=O (Co-O*) form O-O bond complex (Co-OO-Co). On the other hand, in AB mechanism, entropy highly decreases while O-O bond is formed between water molecule in bulk solution and Co=O on the electrode surface by nucleophilic attack of water molecule. As shown in Figure 13b, overall entropic energy barrier ($-T\Delta^\ddagger S$) for AB mechanism was calculated to -0.48 eV, whereas RC mechanism has positive entropic contribution ($T\Delta^\ddagger S = + 0.19$ eV).

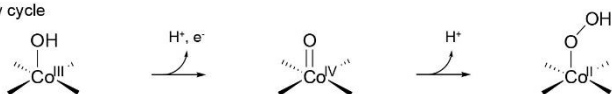
From the previously reported paper, two O-O bond formation pathways are available for Mn₃O₄ NPs as shown in Figure 3.13a. Based on the DFT calculation results and experimentally determined $T\Delta^\ddagger S$ (-0.46 – -0.49 eV), we suggest that OER is proceeded according to AB mechanism on Mn₃O₄ NPs.



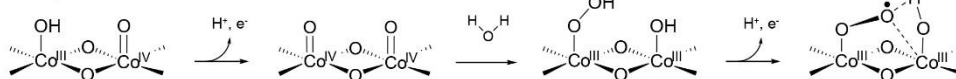
The O-O bond formation mechanism of Co-Pi also can be understood based on our results and reported OER mechanisms of the Co based catalyst. Frei group identified OER mechanisms of Co_3O_4 nanoparticles by time-resolved infrared spectroscopy. As shown in Figure 3.14, two different acid-base mechanisms were suggested on Co_3O_4 nanoparticles depending on the shape of active Co site. It was observed that one-electron transfer takes longer than 300 ms in single Co active site (slow cycle). On the other hand, by stabilization of O-O bond by hydrogen-bond network with adjacent Co-OH group, fast cycle ($\text{TOF} > 3 \text{ s}^{-1}$) was shown in dual Co active site. Considering the reported active site structure of Co-Pi, which is the di-cobalt edge site, OER on the Co-Pi would be proceeded following acid-base mechanism, and cooperative effect such as hydrogen bond network attribute the reduced entropic energy barrier ($T\Delta^\ddagger S = 0.4 \text{ eV}$) compared with calculated entropic barrier for typical acid-base mechanism (0.48 eV). For the Co-Pi film, Nocera group reported that O-O bond can be formed by direct intramolecular coupling between two oxo radicals. More positive entropic contribution ($T\Delta^\ddagger S = -0.4 \text{ eV}$) is also predictable when some of O-O bond formation steps are proceeded following RC mechanisms.

O-O bond formation mechanism of Co_3O_4 NPs

Slow cycle



Fast cycle



O-O bond formation mechanism of Co-Pi

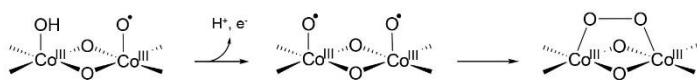


Figure 3.14 Proposed mechanisms of O-O bond formation during OER on cobalt based catalysts. Two types of acid-base mechanisms were reported by Frei group. The one is slow cycle by single Co site and the other is fast cycle by dual Co site. Radical-coupling mechanism was reported by Nocera group.

Chapter 4. Conclusion

Temperature dependent analysis was conducted to measure the activation energy parameters of Mn_3O_4 NPs, and Co-Pi for OER. Through the Eyring plot in this temperature range, activation enthalpy ($\Delta^\ddagger H$) and entropy ($T\Delta^\ddagger S$) were measured successfully. The measured $\Delta^\ddagger H$ linearly decreased with overpotential in proportion to the transfer coefficient (α), which was measured to 0.74, and 0.96 for Mn_3O_4 NPs, and Co-Pi respectively. This linear relation is consistent with Butler-Volmer kinetic model, and measured α was also well matched with previous reported mechanistic understanding of each catalyst. In addition, $T\Delta^\ddagger S$ was successfully measured to -0.46 – -0.49 eV for Mn_3O_4 NPs, and -0.4 eV for Co-Pi at 410 mV overpotential, which take a larger part of the whole activation gibbs free energy ($\Delta^\ddagger G$) than $\Delta^\ddagger H$. Based on the entropy values of intermediate species calculated by DFT studies, we suggest that this negative activation entropy could be possible with nucleophilic attack of H_2O molecule in the process of O-O bond formation.

The here-discussed entropic contribution to electrochemical oxygen evolution reaction suggest that the unfavorable activation entropy ($\Delta^\ddagger S$) would be key factor of activity discrepancy between artificial heterogeneous catalyst and biological PS II system. In this regard, in order to develop highly efficient catalyst competitive to PS II, it is necessary to investigate how entropy contribute to catalysis,

as well as optimize the oxygen binding energy (E_o) of material. We proposed methodology to measuring activation enthalpy ($\Delta^\ddagger H$) and entropy ($\Delta^\ddagger S$) based on temperature dependent analysis. Along with this approach, it is also emphasized to identify the kinetic parameters such as rate constants (k) and the number of active site (Γ_{act}) to measure activation entropy in heterogeneous system. Providing the representative results of Mn_3O_4 NPs and Co-Pi catalyst, we propose the highly negative activation entropy is related to inflow of water molecule which is substrate of O-O bond. We anticipate that the drastic decrease of entropy can be improved by hydrogen-bond network as shown in enzyme catalysis or Co-Pi, and by controlling the transportation of water molecules to electrode surface in an ordered way.

References

1. Seh, Z. W.; Kibsgaard, J.; Dickens, C. F.; Chorkendorff, I.; Nørskov, J. K.; Jaramillo, T. F. Combining theory and experiment in electrocatalysis: Insights into materials design. *Science* **2017**, *355*, 157
2. Kudo, A.; Miseki, Y.; Heterogeneous Photocatalyst Materials for Water Splitting. *Chem. Soc. Rev.* **2009**, *38*, 253–278.
3. U. S. E. I. Administration., **2013**.
4. Surendranath, Y.; Kanan, M. W.; Nocera, D. G. Mechanistic Studies of the Oxygen Evolution Reaction by a Cobalt-Phosphate Catalyst at Neutral pH. *J. Am. Chem. Soc.* **2010**, *132*, 16501–16509
5. Jin, K.; Seo, H.; Hayashi, T.; Balamurugan, M.; Jeong, D, Go, Y. K.; Hong, J. S.; Cho, K. H.; Kakizaki, H.; Bonnet-Mercier, N.; Kim, M. G.; Kim, S. H.; Nakamura, R.; Nam, K. T. Mechanistic Investigation of Water Oxidation Catalyzed by Uniform, Assembled MnO Nanoparticles. *J. Am. Chem. Soc.* **2017**, *139*, 2277–2285
6. Ooka, H.; Takashima, T.; Yamaguchi, A.; Hayashia, T.; Nakamura, R.; Element Strategy of Oxygen Evolution Electrocatalysis Based on in situ Spectroelectrochemistry. *Chem. Commun.* **2017**, *53*, 7149–7161

7. Fang, Y.-H.; Liu, Z.-P. Mechanism and Tafel Lines of Electro-Oxidation of Water to Oxygen on RuO₂(110). *J. Am. Chem. Soc.* **2010**, *132*, 18214–18222
8. Zhang, M.; Respinis, M. D.; Frei, H. Time-Resolved Observations of Water Oxidation Intermediates on a Cobalt Oxide Nanoparticle Catalyst. *Nat. Chem.* **2014**, *6*, 362–367
9. Ullman, A. M.; Brodsky, C. N.; Li, N.; Zheng, S.-L.; Nocera, D. G. Probing Edge Site Reactivity of Oxidic Cobalt Water Oxidation Catalysts. *J. Am. Chem. Soc.* **2016**, *138*, 4229–4236
10. Pham, H. H.; Cheng, M.-J.; Frei, H.; Wang, L.-W. Surface Proton Hopping and Fast-Kinetics Pathway of Water Oxidation on Co₃O₄ (001) Surface. *ACS Catal.* **2016**, *6*, 5610–5617
11. Rossmeisl, J.; Qu, Z. W.; Zhu, H.; Kroes, G. J.; Nørskov, J. K. Electrolysis of Water on Oxide Surfaces. *J. Electroanal. Chem.* **2007**, *607* 83–89
12. Rossmeisl, J.; Logadottir, A.; Nørskov, J. K. Electrolysis of Water on (Oxidized) Metal Surfaces. *Chem. Phys.* **2005**, *319*, 178–184
13. Man, I. C.; Su, H. Y.; Calle-Vallejo, F.; Hansen, H. A.; Martinez, J. I.; Inoglu, N. G.; Kitchin, J.; Jaramillo, T. F.; Nørskov, J. K.; Rossmeisl, J. Universality in Oxygen Evolution Electrocatalysis on Oxide Surfaces. *ChemCatChem* **2011**, *3*, 1159–1165

14. Suntivich, J.; May, K. J.; Gasteiger, H. A.; Goodenough, J. B.; Shao-Horn, Y. A Perovskite Oxide Optimized for Oxygen Evolution Catalysis from Molecular Orbital Principles. *Science* **2011**, *334*, 1383–1385
15. Exner, K. S.; Over, H. Kinetics of Electrocatalytic Reactions from First-Principles: A Critical Comparison with the Ab Initio Thermodynamics Approach. *Acc. Chem. Res.* **2017**, *50*, 1240–1247
16. Umena, Y.; Kawakami, K.; Shen, J. R.; Kamiya, N. Crystal Structure of Oxygen-Evolving Photosystem II at a Resolution of 1.9Å. *Nature* **2011**, *473*, 55–61.
17. Askerka, M.; Brudvig, G. W.; Batista, V. S. The O₂-Evolving Complex of Photosystem II: Recent Insights from Quantum Mechanics/Molecular Mechanics (QM/MM), Extended X-ray Absorption Fine Structure (EXAFS), and Femtosecond X-ray Crystallography Data. *Acc. Chem. Res.* **2017**, *50*, 41–48.
18. Debus, R. J.; Protein Ligation of the Photosynthetic Oxygen-Evolving Center. *Coord. Chem. Rev.* **2008**, *252*, 244–258
19. Hillier, W.; Wydrzynski, T. Substrate Water Interactions within the Photosystem II Oxygen Evolving Complex. *Phys. Chem. Chem. Phys.* **2004**, *6*, 4882–4889.

20. Suga, M.; Akita, F.; Hirata, K.; Ueno, G.; Murakami, H.; Nakajima, Y.; Shimizu, T.; Yamashita, K.; Yamamoto, M.; Ago, H.; Shen, J. R. Native Structure of Photosystem II at 1.95 Å Resolution Viewed by Femtosecond X-ray Pulses. *Nature* **2015**, *517*, 99–105
21. Bao, H.; Burnap, R. L. Structural Rearrangements Preceding Dioxygen Formation by the Water Oxidation Complex of Photosystem II. *Proc. Natl. Acad. Sci. U. S. A.* **2015**, *112*, 6139–6147
22. Pe´rez-Navarro, M.; Neese, F.; Lubitz, W.; Pantazis, D. A.; Cox, N. Recent Developments in Biological Water Oxidation. *Curr. Opin. Chem. Biol.* **2016**, *31*, 113–119
23. Vogt, L.; Vinyard, D. J.; Khan, S.; Brudvig, G. W. Oxygen-Evolving Complex of Photosystem II: An Analysis of Second-Shell Residues and Hydrogen-Bonding Networks. *Curr. Opin. Chem. Biol.* **2015**, *25*, 152–158
24. Pantazis, D. A. Missing Pieces in the Puzzle of Biological Water Oxidation. *ACS Catal.* **2018**, *8*, 9477–9507
25. Rappaport, F.; Ishida, N.; Sugiura, M.; Boussac, A.; Ca²⁺ Determines the Entropy Changes Associated with the Formation of Transition States during Water Oxidation by Photosystem II. *Energy Environ. Sci.* **2011**, *4*, 2520–2524.

- 26 Singh, S.; Debus, R. J.; Wydrzynski, T.; Hillier, W. Investigation of Substrate Water Interactions at the High-Affinity Mn Site in the Photosystem II Oxygen-Evolving Complex. *Philos. Trans. R. Soc. B Biol. Sci.* **2008**, *363*, 1229–1234.
27. Haumann, M.; Liebisch, P.; Muller, C.; Barra, M.; Grabolle, M.; Dau H. Photosynthetic O₂ Formation Tracked by Time-Resolved X-ray Experiments. *Science* **2005**, *310*, 1019–1021
28. Nilsson, H.; Rappaport, F.; Boussac, A.; Messinger, J.; Substrate–Water Exchange in Photosystem II is Arrested Before Dioxygen Formation. *Nat. Commun.* **2014**, *5*, 4305
- 29 Schaleger, L. L.; Long, F. A. Entropies of Activation and Mechanisms of Reactions in Solution. *Adv. Phys. Org. Chem.* **1963**, *1*, 1–33.
- 30 Jencks, W. P. Binding Energy, Specificity, and Enzymic Catalysis: The Circe Effect. *Adv. Enzymol. Relat. Areas Mol. Biol.* **2006**, *43*, 219–410.
- 31 Sievers, A.; Beringer, M.; Rodnina, M. V.; Wolfenden, R. The Ribosome as an Entropy Trap. *Proc. Natl. Acad. Sci. U. S. A.* **2004**, *101*, 7897–7901.
- 32 Trobro, S.; Åqvist, J. Mechanism of peptide bond synthesis on the ribosome. *Proc. Natl. Acad. Sci. U. S. A.* **2005**, *102*, 12395–12400.
- 33 Truong, K.; Su, Y.; Song, J.; Chen, Y. Entropy-Driven Mechanism of an E3 Ligase. *Biochemistry* **2011**, *50*, 5757–5766.

- 34 Page, M. I.; Jencks, W. P. Entropic Contributions to Rate Accelerations in Enzymic and Intramolecular Reactions and the Chelate Effect. *Proc. Natl. Acad. Sci. U. S. A.* **1971**, *68*, 1678–1683.
- 35 Ranaghan, K. E.; Ridder, L.; Szeftczyk, B.; Sokalski, W. A.; Hermann, J. C.; Mulholland, A. J. Transition State Stabilization and Substrate Strain in Enzyme Catalysis: Ab Initio QM/MM Modelling of the Chorismate Mutase Reaction. *Org. Biomol. Chem.* **2004**, *2*, 68–980.
- 36 Kazemi, M.; Åqvist, J. Chemical Reaction Mechanisms in Solution from Brute Force Computational Arrhenius Plots. *Nat. Commun.* **2015**, *6*, 7293.
- 37 Åqvist, J.; Kamerlin, S. C. L. Exceptionally Large Entropy Contributions Enable the High Rates of GTP Hydrolysis on the Ribosome. *Sci. Rep.* **2015**, *5*, 15817.
- 38 Indra, A.; Menezes, P. W.; Zaharieva, I.; Baktash, E.; Pfrommer, J.; Schwarze, M.; Dau, H.; Driess, M. Active Mixed-Valent MnO_x Water Oxidation Catalysts through Partial Oxidation (Corrosion) of Nanostructured MnO Particles. *Angew. Chem., Int. Ed.* **2013**, *52*, 13206–13210.
- 39 Robinson, D. M.; Go, Y. B.; Greenblatt, M.; Dismukes, G. C. Water Oxidation by λ -MnO₂: Catalysis by the Cubical Mn₄O₄ Subcluster

Obtained by Delithiation of Spinel LiMn_2O_4 . *J. Am. Chem. Soc.* **2010**, 132, 11467-11469

- 40** Zaharieva, I.; Najafpour, M.M.; Wiechen, M.; Haumann, M.; Kurz, P.; Dau, H. Synthetic manganese–calcium oxides mimic the water-oxidizing complex of photosynthesis functionally and structurally. *Energy Environ. Sci.* **2011**, 4, 2400-2408
- 41** Jin, K.; Park, J.; Lee, J.; Yang, K. D.; Pradhan, G. K.; Sim, U.; Jeong, D.; Jang, J. L.; Park, S.; Kim, D.; Sung, N-E.; Kim, S. H.; Han, S.; Nam, K. T. Hydrated Manganese(II) Phosphate ($\text{Mn}_3(\text{PO}_4)_2 \cdot 3\text{H}_2\text{O}$) as a Water Oxidation Catalyst. *J. Am. Chem. Soc.* **2014**, 136, 7435-7443
- 42** Park, J.; Kim, H.; Jin, K.; Lee, B. J.; Park, Y-S.; Kim, H.; Park, I.; Yang, K. D.; Jeong, H-Y.; Kim, J.; Hong, K. T.; Jang, H. W.; Kang, K.; Nam, K. T. A New Water Oxidation Catalyst: Lithium Manganese Pyrophosphate with Tunable Mn Valency. *J. Am. Chem. Soc.* **2014**, 136, 4201-4211
- 43** Jin, K.; Chu, A.; Park, J.; Jeong, D.; Jerng, S. E.; Sim, U.; Jeong, H.-Y.; Lee, C. W.; Park, Y.-S.; Yang, K. D.; Pradhan, G. K.; Kim, D.; Sung, N.-E.; Kim, S. H.; Nam, K. T. Partially Oxidized Sub-10 nm MnO Nanocrystals with High Activity for Water Oxidation Catalysis. *Sci. Rep.* **2015**, 5, 10279

- 44 Montoya, J. H.; Doyle, A. D.; Nørskov, J. K.; Vojvodic, A. Trends in adsorption of electrocatalytic water splitting intermediates on cubic ABO₃ oxides. *Phys. Chem. Chem. Phys.* **2018**, 20, 3813-3818
- 45 Li, M.; Zhang, L.; Xu, Q.; Niu, J.; Xia, Z. N-doped graphene as catalysts for oxygen reduction and oxygen evolution reactions: Theoretical considerations. *J. Catal.* **2014**, 314, 66–72
- 46 Kim, H.; Park, J.; Park, I.; Jin, K.; Jerng, S. E.; Kim, S. H.; Nam, K. T.; Kang, K. Coordination tuning of cobalt phosphates towards efficient water oxidation catalyst. *Nat. Commun.* **2015**, 6, 8253
- 47 Mom, R. V.; Cheng, J.; Koper, M. T. M.; Sprik, M. Modeling the Oxygen Evolution Reaction on Metal Oxides: The Influence of Unrestricted DFT Calculations. *J. Phys. Chem. C* **2014**, 118, 8, 4095-4102
48. Nurlaela, E.; Shinagawa, T.; Qureshi, M.; Dhawale, D. S.; Takanebe, K. Temperature Dependence of Electrocatalytic and Photocatalytic Oxygen Evolution Reaction Rates Using NiFe Oxide. *ACS Catal.* **2016**, 6, 1713–1722
- 49 Zhang, B.; Zheng, X.; Voznyy, O.; Comin, R.; Bajdich, M.; García-Melchor, M.; Han, L.; Xu, J.; Liu, M.; Zheng, L.; Arquer, F. P. G. de; Dinh, C. T.; Fan, F.; Yuan, M.; Yassitepe, E.; Chen, N.; Regier, T.; Liu, P.; Li, Y.; Luna, P. D.; Janmohamed, A.; Xin, H. L.; Yang, H.; Vojvodic, A.; Sargent,

- E. H. Homogeneously dispersed multimetal oxygen-evolving catalysts. *Science* **2016**, 352, 333-337
- 50.** Swierk, J. R.; Klaus, S.; Trotochaud, L.; Bell, A. T.; Tilley, T. D. Electrochemical Study of the Energetics of the Oxygen Evolution Reaction at Nickel Iron (Oxy)Hydroxide Catalysts. *J. Phys. Chem. C* **2015**, 119, 19022–19029
- 51.** Miles, M. H.; Kissel, G.; Lu, P. W. T.; Srinivasan, S. Effect of Temperature on Electrode Kinetic Parameters for Hydrogen and Oxygen Evolution Reactions on Nickel Electrodes in Alkaline Solutions. *J. Electrochem. Soc.* **1976**, 123, 332–336
- 52.** Davidson, C.; Kissel, G.; Srinivasan, S. Electrode Kinetics of the Oxygen Evolution Reaction at NiCo₂O₄ from 30% KOH.: Dependence on Temperature. *J. Electroanal. Chem. Interfacial. Electrochem.* **1982**, 132, 129–135
- 53.** Wakabayashi, N.; Takeichi, M.; Itagaki, M.; Uchida, H.; Watanabe, M. Temperature-Dependence of Oxygen Reduction Activity at a Platinum Electrode in an Acidic Electrolyte Solution Investigated with a Channel Flow Double Electrode. *J. Electroanal. Chem.* **2005**, 574, 339–346

54. Wakabayashi, N.; Takeichi, M.; Uchida, H.; Watanabe, M. Temperature Dependence of Oxygen Reduction Activity at Pt-Fe, Pt-Co, and Pt-Ni Alloy Electrodes. *J. Phys. Chem. B* **2005**, *109*, 5836–5841
55. Markovic, N. M.; Grgur, B. N.; Ross, P. N. Temperature-Dependent Hydrogen Electrochemistry on Platinum Low-Index Single-Crystal Surfaces in Acid Solutions. *J. Phys. Chem. B* **1997**, *101*, 5405–5413
56. Sohrabnejad-Eskan, I.; Goryachev, A.; Exner, K. S.; Kibler, L. A.; Hensen, E. J. M.; Hofmann, J. P.; Over, H. Temperature-Dependent Kinetic Studies of the Chlorine Evolution Reaction over RuO₂(110) Model Electrodes. *ACS Catal.* **2017**, *7*, 2403–2411
57. Chen, G.; Lam, W. W. Y.; Lo, P. K.; Man, W. L.; Chen, L.; Lau, K. C.; Lau, T.-C.; Mechanism of Water Oxidation by Ferrate(VI) at pH 7–9. *Chem. Eur. J.* **2018**, *24*, 1–9
58. Savini, A.; Bucci, A.; Bellachioma, G.; Rocchigiani, L.; Zuccaccia, C.; Llobet, A.; Macchioni, A.; Mechanistic Aspects of Water Oxidation Catalyzed by Organometallic Iridium Complexes. *Eur. J. Inorg. Chem.* **2014**, *4*, 690–697
59. Codolà, Z.; Cardoso, J. M. S.; Royo, B.; Costas, M.; Lloret-Fillol, J. Highly Effective Water Oxidation Catalysis with Iridium Complexes through the Use of NaIO₄. *Chem. Eur. J.* **2013**, *19*, 7203–7213

60. Tong, L.; Inge, A. K.; Duan, L.; Wang, L.; Zou, X.; Sun, L. Catalytic Water Oxidation by Mononuclear Ru Complexes with an Anionic Ancillary Ligand. *Inorg. Chem.* **2013**, *52*, 2505–2518
61. Oloo, W. N.; Fielding, A. J.; Que Jr., L. Rate-Determining Water-Assisted O–O Bond Cleavage of an Fe^{III}-OOH Intermediate in a Bio-inspired Nonheme Iron-Catalyzed Oxidation. *J. Am. Chem. Soc.* **2013**, *135*, 6438–6441
62. Liu, L. V.; Hong, S.; Cho, J.; Nam, W.; Solomon, E. I. Comparison of High-Spin and Low-Spin Nonheme Fe^{III}-OOH Complexes in O–O Bond Homolysis and H-Atom Abstraction Reactivities. *J. Am. Chem. Soc.* **2013**, *135*, 3286–3299
63. Eyring, H. The Activated Complex and the Absolute Rate of Chemical Reactions. *Chem. Review.* **1935**, *17*, 65–77
64. Bockris, J. O'M.; Reddy, A. K. N. *Modern Electrochemistry*; Plenum/Rosetta Publication: New York, **1973**; Vol. 2.
65. Ooka, H.; Yamaguchi, A.; Takashima, T.; Hashimoto, K.; Nakamura, R. Efficiency of Oxygen Evolution on Iridium Oxide Determined from the pH Dependence of Charge Accumulation. *J. Phys. Chem. C* **2017**, *121*, 17873–17881

66. Bergmann, A.; Martinez-Moreno, E.; Teschner, D.; Chernev, P.; Gliech, M.; de Araújo, J. F.; Reier, T.; Dau, H.; Strasser, P. Reversible Amorphization and the Catalytically Active State of Crystalline Co_3O_4 during Oxygen Evolution. *Nat. Commun.* **2015**, *6*, 8625
67. Ahn H. S.; Bard, A. J. Surface Interrogation of CoPi Water Oxidation Catalyst by Scanning Electrochemical Microscopy. *J. Am. Chem. Soc.* **2015**, *137*, 612–615
68. Ahn, H. S.; Bard, A. J. Switching Transient Generation in Surface Interrogation Scanning Electrochemical Microscopy and Time-of-Flight Techniques. *Anal. Chem.* **2015**, *87*, 12276–12280

국문 초록

인공 광합성은 지속 가능한 에너지 생산을 위한 중요한 전략 중 하나이다. 인공 광합성에서 중요한 부분인 산소 발생 반응은, 고 에너지 장벽으로 인해 반응 속도가 매우 느리며, 이에 따라 고 활성 촉매의 개발이 필수적이다. 현재까지, 고 에너지 장벽에서 활성 엔탈피 ($\Delta^\ddagger H$)의 기원은 깊게 이해되어 왔고, 활성 엔탈피를 감소시키기 위한 다양한 전략이 제시되어 왔다. 이러한 접근법에서, 반응 중 중간 생성물 (*O, *OH, *OOH)과의 결합 에너지 조절을 중심으로 촉매 개발이 진행되어 왔지만, 현재 전기화학 촉매 성질은 자연계의 산소 발생 효소인 PS II 의 특성과 비교하여 현저히 떨어지는 상황이며, 결합 에너지 조절을 통한 특성 향상에는 이론적인 한계점이 존재한다.

자연계에서 이루어지는 생화학 반응은 효소에 의해 진행되는데, 효소는 반응의 활성화 에너지 장벽을 낮추어 반응 속도를 크게 증가시키는 역할을 한다. 이러한 효소 작용에 대한 기원은 반응 친화적인 활성화 엔트로피 ($\Delta^\ddagger S$)로 규명되어왔다. 물 산화 반응에서, 망간 칼슘 클러스터의 칼슘 이온 (Ca^{2+}) 및 아미노산 잔기에 의한 유리한 엔트로피 효과가 빠른 반응 속도에 결정적인 역할을 한다고 보고 되었으며, 이러한 이해를 바탕으로 분자 촉매에서의 엔트로피 기여 또한 활발히 연구되고 있다. 그러나 이중 시스템에서의 물 분해 반응에서는,

활성화 엔트로피 측정 및 계산의 어려움으로 인해 엔트로피의 효과 또는 기원은 분명하게 이해되지 않았으며 그 중요성이 간과되고 있다.

이 연구에서, 우리는 온도 의존성 분석을 통해 Mn_3O_4 나노 입자 및 Co-Pi 촉매의 물 산화 반응에 대한 엔트로피 기여를 조사하였다. 또한, 전달 계수 (α), 활성화 엔탈피를 기반으로 촉매 반응을 이해하였다. 활성화 엔탈피가 전달 계수에 비례하여 과전압에 따라 감소하는 것을 확인하였으며, Mn_3O_4 나노 입자 및 Co-Pi 촉매의 α 는 각각 0.74, 0.96 로 측정되었다. 이는 각 촉매에 대해 이전에 보고된 메커니즘 해석과 일치하는 결과이다. 이외에도, 온도 의존성 분석을 통해 엔트로피 기여를 측정하였으며, Mn_3O_4 나노 입자의 경우 $T\Delta^\ddagger S$ 는 -0.46 에서 -0.49 eV 범위로 측정되었고, Co-Pi 촉매의 경우 -0.4 eV 로 측정되었다. 이는 전체 활성화 깃스 에너지에서 $\Delta^\ddagger H$ 보다 큰 비중을 차지하는 결과이다. DFT 연구에 의해 계산된 엔트로피 값을 고려했을 때, 이러한 큰 활성화 엔트로피는 O-O 결합 형성 과정에서 물 분자의 뉴클레오펠릭 어택으로 인한 엔트로피 감소로 설명 가능하다. 우리는 엔트로피 기여 규명을 통해 Mn_3O_4 나노 입자 및 Co-Pi 촉매의 물 산화 반응 메커니즘이 Acid-base 메커니즘을 따른다는 것을 제안하였다. 더 나아가, Co-Pi 촉매의 경우 활성 사이트의 Co-OOH 와 그와 인접한 Co-OH 사이의 수소 결합이 O-O 결합을 안정화 시키며,

그로 인해 엔트로피 장벽이 감소할 수 있음을 확인하였다.

주요어: 산소 발생 반응, 전이 상태 이론, 온도 의존성 분석, 전기화학 분석, 엔트로피, O-O 결합, 망간 산화물, 코발트 포스페이트

학번: 2017-24770